

# The CO-H<sub>2</sub> Conversion Factor in Disc Galaxies and Mergers

Desika Narayanan<sup>1\*†</sup>, Mark Krumholz<sup>2</sup>, Eve C. Ostriker<sup>3</sup>, Lars Hernquist<sup>4</sup>

<sup>1</sup>*Steward Observatory, University of Arizona, 933 N Cherry Ave, Tucson, Az, 85721*

<sup>2</sup>*Department of Astronomy and Astrophysics, University of California, Santa Cruz, CA, 95064*

<sup>3</sup>*Department of Astronomy, University of Maryland, College Park, 20742*

<sup>4</sup>*Harvard-Smithsonian Center for Astrophysics, 60 Garden St., Cambridge, Ma 02138*

Accepted by MNRAS

## ABSTRACT

Relating the observed CO emission from giant molecular clouds (GMCs) to the underlying H<sub>2</sub> column density is a long-standing problem in astrophysics. While the Galactic CO-H<sub>2</sub> conversion factor ( $X_{\text{CO}}$ ) appears to be reasonably constant, observations indicate that  $X_{\text{CO}}$  may be depressed in high-surface density starburst environments. Using a multi-scale approach, we investigate the dependence of  $X_{\text{CO}}$  on the galactic environment in numerical simulations of disc galaxies and galaxy mergers.  $X_{\text{CO}}$  is proportional to the GMC surface density divided by the integrated CO intensity,  $W_{\text{CO}}$ , and  $W_{\text{CO}}$  is related to the kinetic temperature and velocity dispersion in the cloud. In disc galaxies (except within the central  $\sim$  kpc), the galactic environment is largely unimportant in setting the physical properties of GMCs provided they are gravitationally bound. The temperatures are roughly constant at  $\sim 10$  K due to the balance of CO cooling and cosmic ray heating, giving a nearly constant CO-H<sub>2</sub> conversion factor in discs. In mergers, the velocity dispersion of the gas rises dramatically during coalescence. The gas temperature also rises as it couples well to the warm ( $\sim 50$  K) dust at high densities ( $n > 10^4 \text{ cm}^{-3}$ ). The rise in velocity dispersion and temperature combine to offset the rise in surface density in mergers, causing  $X_{\text{CO}}$  to drop by a factor of  $\sim 2 - 10$  compared to the disc simulation. This model predicts that high-resolution ALMA observations of nearby ULIRGs should show velocity dispersions of  $10^1$ - $10^2 \text{ km s}^{-1}$ , and brightness temperatures comparable to the dust temperatures.

**Key words:** ISM: molecules - ISM: clouds - galaxies:ISM - galaxies:starburst - galaxies:star formation - galaxies:interactions

## 1 INTRODUCTION

Stars form in giant molecular clouds (GMCs) whose primary constituent is molecular hydrogen, H<sub>2</sub>. Because H<sub>2</sub> lacks a permanent dipole moment, and the lowest lying excited state capable of quadrupole emission requires temperatures  $\sim 500$  K to be excited, the physical conditions in the cold ( $\sim 10$  K) molecular gas are typically probed via tracer molecules, rather than by direct detection of H<sub>2</sub>.

Carbon Monoxide ( $^{12}\text{C}^{16}\text{O}$ ; hereafter, CO) is the second most abundant molecule in GMCs. Because the J=1-0 rotational transition of CO lies only  $\sim 5$  K above ground, has a relatively low effective density ( $\sim 10^{2-3} \text{ cm}^{-3}$ ) for excitation (Evans 1999), and has a wavelength of  $\sim 3$  mm which is readily observable from the ground, CO (J=1-0) has historically been one of the most commonly used tracers of physical conditions in the molecular ISM.

A large uncertainty in using CO to trace H<sub>2</sub> gas is relating the observed CO line luminosity to the underlying H<sub>2</sub> column density. However, despite the fact that CO/H<sub>2</sub> abundances vary strongly within GMCs (e.g. Sternberg & Dalgarno 1995; Lee et al. 1996; Hollenbach & Tielens 1999; Glover et al. 2010; Glover & Mac Low 2011), a multitude of observations suggests that the conversion factor between CO and H<sub>2</sub> is reasonably constant in Galactic GMCs, following the relation:

$$X_{\text{CO}} = 2 - 4 \times 10^{20} \text{ cm}^{-2} / (\text{K} - \text{km s}^{-1}) \quad (1)$$

where  $X_{\text{CO}}$  is the CO-H<sub>2</sub> conversion factor in units of H<sub>2</sub> column density divided by velocity-integrated CO line intensity<sup>1</sup>. Lines of evidence for a relatively constant  $X_{\text{CO}}$  include comparisons between CO luminosities and molecular column densities determined via a variety of techniques, including dust extinction (Dickman 1975),  $\gamma$ -ray emission (Bloemen et al. 1986; Strong & Mattox

\* E-mail: dnanayanan@as.arizona.edu

† Bart J. Bok Fellow

<sup>1</sup>  $X_{\text{CO}}$  is sometimes referred to in the literature as the “X-factor”. We will use  $X_{\text{CO}}$  and X-factor interchangeably.

1996; Abdo et al. 2010b) and thermal dust emission (Dame et al. 2001; Draine et al. 2007).

Beyond this, the CO-H<sub>2</sub> conversion factor appears to have the same relatively narrow range of values in galaxies in the Local Group as well (Blitz et al. 2007; Wolfire et al. 2010), though there may be some variations associated with metallicity (Wilson 1995; Arimoto et al. 1996; Boselli et al. 2002; Rosolowsky et al. 2003; Israel 2005; Bell et al. 2006; Leroy et al. 2006; Bell et al. 2007; Bolatto et al. 2008; Leroy et al. 2011). The relatively narrow distribution of values for  $X_{\text{CO}}$  in Local Group GMCs<sup>2</sup> may arise from the fact that molecular clouds appear have remarkably similar physical properties in both the Milky Way and nearby galaxies. GMCs in the Galaxy and local Universe appear to have a nearly constant surface density of 85-100 M<sub>☉</sub>/pc<sup>2</sup>, obey the size-linewidth relation, and have relatively low kinetic temperatures of 10-20 K (Solomon et al. 1987; Blitz et al. 2007; Heyer et al. 2009). Magnetohydrodynamic and radiative transfer modeling by Glover et al. (2010), Glover & Mac Low (2011) and Shetty et al. (2011a,b) have shown that simulated GMCs with mean densities, sizes, velocity dispersions, and metallicities comparable to those found in the Galaxy naturally produce  $X_{\text{CO}}$  conversion factors comparable to Equation 1.

The situation becomes more complex in starburst galaxies. By utilising high-spatial resolution interferometric mapping of nearby (ultra)luminous infrared galaxies ([U]LIRGs;  $L_{\text{IR}} > [10^{12}]10^{11} L_{\odot}$ ), Solomon et al. (1997), Downes & Solomon (1998) and Downes & Solomon (2003) have shown that the application of the “standard” Galactic  $X_{\text{CO}}$  conversion factor would cause the inferred molecular gas mass to exceed the dynamical mass in these galaxies. In this case, the constraints on  $X_{\text{CO}}$  are in the range  $\sim 2 - 10 \times 10^{19} \text{cm}^{-2}/\text{K} - \text{km/s}$ : a factor of 2-20 lower than the Galactic value. Other observational evidence from local starbursts (Hinz & Rieke 2006; Meier et al. 2010), the Galactic centre (Oka et al. 1998) and high- $z$  submillimetre-galaxies (Tacconi et al. 2008) have all corroborated this picture that  $X_{\text{CO}}$  may be lower in regions of high molecular surface density.

The exact origin of a lower  $X_{\text{CO}}$  factor in starburst galaxies is not entirely clear. Models by Maloney & Black (1988) which predate the aforementioned observations, predicted that warmer molecular gas temperatures in infrared-luminous galaxies may drive a lower  $X_{\text{CO}}$  conversion factor due to an increase in CO brightness temperature with kinetic temperature in optically thick clouds. Alternatively, Downes & Solomon (1998) suggest that the CO line width in starbursts traces a combination of the gaseous and stellar potential, rather than just the H<sub>2</sub> mass. In the case where CO is optically thick, the observed velocity-integrated CO line intensity can increase with the velocity dispersion. Maloney & Black (1988) and Shetty et al. (2011b) also postulated a similar effect if the CO linewidths were larger than their typical virial values.

While the scaling of  $X_{\text{CO}}$  with environmental parameters is not yet known, the ramifications are profound. For example, if  $X_{\text{CO}}$  does indeed systematically vary in higher surface density environments, our current understanding of the normalisation and index of the Kennicutt-Schmidt star formation rate-gas surface density relation in star forming galaxies may change (Kennicutt 1998a; Daddi et al. 2010; Genzel et al. 2010). At higher redshifts, as high gas sur-

face density galaxies begin to contribute substantially to the cosmic star formation rate density (e.g. Le Floch et al. 2005; Hopkins et al. 2010; Hopkins & Hernquist 2010), the variation of  $X_{\text{CO}}$  with environment may affect observed values of the cosmic evolution of  $\Omega_{\text{H}_2}$ . More generally, the interpretation of forthcoming results from the EVLA and ALMA will be severely crippled without an understanding for how to relate the observed CO line flux to the quantity of interest: H<sub>2</sub> gas mass.

In this area, numerical simulations can offer some guidance. Indeed, understanding the origin of  $X_{\text{CO}}$  in galaxies is difficult in that many of the physical parameters driving the relation are coupled. The CO-H<sub>2</sub> conversion factor,  $X_{\text{CO}}$ , has dimensions of:

$$X_{\text{CO}} \propto \Sigma/(W_{\text{CO}}) \propto \Sigma/(\sigma \times T_{\text{B}}) \quad (2)$$

where  $W_{\text{CO}}$  is the velocity-integrated CO intensity,  $\Sigma$  is the gas surface density,  $T_{\text{B}}$  is the brightness temperature of the line, and  $\sigma$  is the velocity dispersion. To first order,  $T_{\text{B}}$  is related to the kinetic temperature of the gas ( $T_{\text{k}}$ ) when the line is thermalised. However, the kinetic temperature of the gas can depend on molecular abundances, gas densities, dust temperatures and the background radiation field (e.g. Narayanan et al. 2006b; Krumholz et al. 2011). The same physical processes which can cause changes in these parameters may also cause the GMC surface densities to change as well. The problem is well-suited for numerical simulations.

Building on the seminal work of Maloney & Black (1988) and more recent simulations of Glover et al. (2010); Glover & Mac Low (2011) and Shetty et al. (2011a,b), we present the first models investigating the CO-H<sub>2</sub> conversion factor in hydrodynamic simulations of isolated disc galaxies and disc galaxy mergers. This is the first paper in a series. In this work, we aim to understand whether  $X_{\text{CO}}$  varies between “normal” disc galaxies and galaxy mergers, and if so, why. In order to do this, we couple smoothed-particle hydrodynamic simulations of galaxies in evolution with dust and molecular line radiative transfer calculations to self-consistently calculate the kinetic temperature of and emissivity from GMCs in our models. Our main result is that higher kinetic temperatures and velocity dispersions in the GMCs naturally arise during mergers, and contribute to lower values of  $X_{\text{CO}}$  in these systems.

Our paper is organised as follows: In § 2, we present our radiative transfer and hydrodynamics methodology; in § 3, we discuss the synthetic observational and physical properties of our model galaxies in an effort to aid comparisons to observations; in § 4, we discuss how the CO-H<sub>2</sub> conversion factor varies in disc galaxies and mergers in our models; in § 5, we discuss the implications of our findings, and in § 6 we summarise our results.

## 2 METHODS

Our goal is to simulate the emission from GMCs on galaxy-wide scales. This involves simulating galaxies in evolution, the physical state of GMCs, molecular line radiative transfer through the clouds, and dust and molecular line radiative transfer through the galaxy. In this section, we describe these simulations, and the relevant assumptions that go into our modeling. This involves combining a large number of simulation codes. In light of this, to guide the reader through the numerical details and equations in this section, we first summarise them more generally here.

We first simulate the hydrodynamic evolution of both disc galaxies and mergers. It is from these simulations that we know the global distribution of stars, gas and metals in the galaxy, and

<sup>2</sup>  $X_{\text{CO}}$  also appears to be reasonably constant in diffuse H<sub>2</sub> gas in the Galaxy (Liszt et al. 2010). This has been attributed to the offsetting effects of lower CO abundances with respect to H<sub>2</sub> (most of the carbon is in C<sup>+</sup>) and a large  $W_{\text{CO}}/N_{\text{CO}}$  ratio in low extinction gas. See the discussion in Pety et al. (2011) for more details.

their physical properties. The radiative transfer occurs in post-processing. We project the physical conditions of the particles onto an adaptive mesh using the SPH smoothing kernel. The base mesh is  $5^3$  spanning a 200 kpc box. The cells refine recursively into  $2^3$  subcells based on the refinement criteria the relative density variations of metals ( $\sigma_{\rho m} / < \rho_m >$ ) should be less than 0.1, and the V-band optical depth across a cell be less than unity. The maximum refinement level was 11, such that the smallest cells in this mesh are of order  $\sim 70$  pc across.

The surface density of and velocity dispersion within the GMCs are set by the physical conditions in the hydrodynamic galaxy evolution simulations. A subgrid prescription comes into play when GMCs are unresolved (i.e. when cells in the adaptive mesh are very large). We assume that all of the  $\text{H}_2$  mass in the cell is in the GMC and we calculate the  $\text{HI-H}_2$  balance via analytic models (described below). From this, the complete physical conditions (except for the temperature) of the GMCs are described by the hydrodynamic galaxy evolution simulations. The temperatures of the clouds are calculated by assuming thermal equilibrium between gas heating (by the grain photoelectric effect and cosmic rays), gas cooling (via molecular and atomic line cooling), dust heating (from the ambient radiation field), thermal dust cooling, and some energy exchange between gas and dust.

With the physical properties of the galaxies and GMCs known, we then proceed to calculate the emergent CO emission from the clouds. We calculate the CO line emission from the GMCs utilising an escape probability formalism. The radiation from these clouds then interacts with other clouds in the galaxy, and the level populations of CO are calculated by the balance of radiative absorptions, stimulated emission, spontaneous emission, and collisions with  $\text{H}_2$  and He.

At this point, the general reader should be equipped to understand the general results of this paper. For the remainder of this section, we elaborate on this abbreviated description. Throughout, we assume  $h = 0.7$ .

## 2.1 Smoothed Particle Hydrodynamic Simulations of Galaxies in Evolution

We simulate the hydrodynamic evolution of both idealised isolated disc galaxies, and mergers between these discs. The purpose of the hydrodynamic simulations is to calculate the spatial distribution of the neutral ISM, stars and metals. It is from the neutral ISM that we will calculate the molecular gas properties, and, as we will discuss, the radiation from the stars and dust in the metals that determine the IR radiation field. Here, we describe the components of the model most pertinent to this study, namely the physics of the ISM and star formation prescriptions. For a more full understanding of the underlying algorithms in GADGET-3, please refer to Springel & Hernquist (2002, 2003); Springel (2005) and Springel et al. (2005b)<sup>3</sup>.

The galaxies are simulated with a modified version of the publicly available SPH code, GADGET-3 (Springel 2005). The ISM is modeled as two-phase, with cold clouds embedded in a hot, pressure-confining medium (McKee & Ostriker 1977; Springel &

Hernquist 2003). Numerically, this is realised via hybrid SPH particles. The cold gas mass grows via radiative cooling of the hot phase, and cold gas is converted to hot gas through the heating associated with star formation.

Stars form in the cold ISM according to a relation  $\text{SFR} \propto \rho_{\text{cold}}^{1.5}$ . The normalisation of this relation is set in order to match the local  $\Sigma_{\text{SFR}} - \Sigma_{\text{gas}}$  relation (Kennicutt 1998a,b; Springel 2000; Cox et al. 2006b).

Supernova pressurisation of the ISM is modeled via an “effective” equation of state (see Figure 4 of Springel et al. 2005b). Here, we assume a modest pressurisation of  $q_{\text{EOS}} = 0.25$  in the Springel et al. (2005b) formalism. This corresponds to a mass-weighted ISM temperature of  $\sim 10^{4.5}$  K. In the Appendix we relax the star formation and equation of state assumptions in order to test the validity of our results.

The simulations here are not cosmological: the discs are set up in an idealised manner in order to maximise spatial resolution. Here, the gravitational softening length for baryons is  $100 \text{ h}^{-1} \text{ pc}$ , and  $200 \text{ h}^{-1} \text{ pc}$  for dark matter. The discs are initialised according to the Mo et al. (1998) formalism, and are bulgeless. They are embedded in dark matter halos with Hernquist (1990) density distributions.

In order to compare with observations in a meaningful manner, we aim to simulate galaxies comparable to those found in the local Universe. Accordingly, our isolated discs are initialised inside haloes of mass  $\sim 1.9 \times 10^{12} M_{\odot}$ , baryonic mass of  $\sim 8 \times 10^{10} M_{\odot}$ , circular velocity of  $160 \text{ km s}^{-1}$ , and with 40% of the baryons in the form of gas.

The mergers are binary 1:1 mergers between discs constructed in the same manner. We simulate three mergers of slightly higher mass in order to ensure that they undergo a luminous starburst comparable to the most extreme ones seen in the local Universe ( $\sim 100 M_{\odot} \text{ yr}^{-1}$ ). In particular, the discs that comprise the binary mergers have a rotation speed of  $225 \text{ km s}^{-1}$ , halo mass of  $\sim 5 \times 10^{12} M_{\odot}$ , and baryonic mass of  $\sim 2.2 \times 10^{11} M_{\odot}$ . The mergers are set on an orbit with angles  $(\theta_1, \phi_1, \theta_2, \phi_2) = (30, 60, -30, 45)$ ,  $(-109, -30, 71, -30)$  and  $(0, 0, 0, 0)$ . The angles for the first two orbits are arbitrary, and were chosen to represent relatively “normal” orbits in our library of simulations. The last merger is a coplanar one, and represents an extreme starburst with an extended duration, which we include simply for comparison. We choose the first merger as our “fiducial” merger for the remainder of this paper as this particular model is well-studied in the literature<sup>4</sup>, and focus particularly on the snapshot when the star formation rate is at its peak. The results from all simulations are similar, and we discuss the minor differences that do exist when necessary.

## 2.2 Physical Properties of Giant Molecular Clouds

We assume that the entire neutral mass in a given cell is locked in a cloud which is spherical, isothermal, and of constant density. We determine the surface density of the neutral gas via

$$\Sigma_{\text{cloud}} = \max(\Sigma_{\text{cell}}, 100 M_{\odot} \text{ pc}^{-2}) \quad (3)$$

where  $\Sigma_{\text{cell}}$  is the surface density of the cell in the SPH simulation. In this model, when the cloud is resolved, we use the surface density as calculated in the simulations. When the cloud is unresolved, we adopt a subresolution surface density comparable to observed

<sup>3</sup> We note that Springel et al. (2005b) describes the publicly-available GADGET-2, whereas the work in this paper utilises GADGET-3, a non-public modified version of GADGET-2. The main improvement in GADGET-3 over GADGET-2 is better load balancing on parallel processors.

<sup>4</sup> In § 3, we discuss the physical and simulated observational properties of our fiducial merger to highlight its similarity to observed local galaxies.

values of GMCs (e.g. Solomon et al. 1987; Blitz & Rosolowsky 2006).

We then determine the  $\text{H}_2$  fraction of the neutral ISM utilising the analytic formalism of Krumholz et al. (2008, 2009a) and McKee & Krumholz (2010). This prescription aims to model the balance between the dissociation of molecules by Lyman-Werner band photons, and the formation of molecules on dust grains. We refer the readers to the aforementioned papers for the full derivation, and simply repeat the numerical prescription here. The molecular fraction is given by:

$$f_{\text{H}_2} \approx 1 - \frac{3}{4} \frac{s}{1 + 0.25s} \quad (4)$$

for  $s < 2$  and  $f_{\text{H}_2} = 0$  for  $s \geq 2$ .  $s = \ln(1 + 0.6\chi + 0.01\chi^2)/(0.6\tau_c)$ , where  $\chi = 0.76(1 + 3.1Z^{0.365})$ , and  $\tau_c = 0.066\Sigma_{\text{cloud}}/(\text{M}_{\odot} \text{pc}^{-2}) \times Z'$ .  $Z'$  is the metallicity divided by the solar metallicity. This formalism for deriving  $f_{\text{H}_2}$  assumes chemical equilibrium.

It is worth a quick note that there are numerous prescriptions for determining the  $\text{H I}/\text{H}_2$  balance in the ISM of simulations, some of which include time-dependent chemistry. Blitz & Rosolowsky (2006) developed an empirical pressure-based methodology for calculating the  $\text{H}_2$  fraction in the neutral ISM, based on observations of local galaxies. Similarly, both semi-analytic models (Obreschkow et al. 2009; Obreschkow & Rawlings 2009), as well as full numerical solutions exist which model the effect of dissociating photons through models of galaxies (e.g. Pelupessy et al. 2006; Dobbs et al. 2008; Robertson & Kravtsov 2008; Pelupessy & Papadopoulos 2009; Gnedin et al. 2009; Gnedin & Kravtsov 2010). We motivate our usage of the analytic prescription of Krumholz et al. (2009a) for two reasons. First, some observational evidence suggests that on small scales ( $< 100$  pc), Equation 4 may fare better than pressure-based prescriptions in describing the state of the neutral ISM in low-metallicity dwarf galaxies (Fumagalli et al. 2010). Second, a comparison between Equation 4 and a numerical treatment of time-dependent chemical reaction network and radiative transfer in galaxies suggests that the analytic approximation is reasonable at metallicities above  $0.01 Z_{\odot}$  (Krumholz & Gnedin 2011). Because we aim to model actively star-forming systems in this work, we find that the mass-weighted metallicity of our model clouds is always higher than this fiducial value and expect that the analytic approximation is therefore reasonable.

With  $\Sigma_{\text{cloud}}$  and  $M_{\text{H}_2}$  defined, the radius of the cloud is known. In order to account for the turbulent compression of gas, we scale the volumetric densities of the GMCs by a factor  $e^{\sigma_p^2/2}$  where numerical simulations show

$$\sigma_p^2 \approx \ln(1 + 3M_{1\text{D}}^2/4) \quad (5)$$

where  $M_{1\text{D}}$  is the 1 dimensional Mach number<sup>5</sup> of the turbulence (Ostriker et al. 2001; Padoan & Nordlund 2002, see also Lemaster & Stone (2008)). Because the temperature calculation is dependent on the density of the GMC (see below), solving for the density and temperature simultaneously is a computationally lengthy process for the multi-million-cell grids that concern us. Thus, to calculate the turbulence-driven density enhancement, we assume the temperature of the GMC is 10 K, which as we shall show, is a good approximation for the bulk of the GMCs in these simulations.

<sup>5</sup> We note that other authors have found a range of possible forms for Equation 5. For example, Lemaster & Stone (2008) find  $\sigma_p^2 \approx 0.6\ln(1 + 0.5M_{3\text{D}}^2)$ , while Price et al. (2011) find  $\sigma_p^2 \approx \ln(1 + 1/9(M_{3\text{D}}^2))$  where  $M_{3\text{D}}$  is the 3D Mach number.

We calculate the 1D velocity dispersion in the cloud:

$$\sigma = \max(\sigma_{\text{cell}}, \sigma_{\text{vir}}) \quad (6)$$

where  $\sigma_{\text{cell}}$  is the mean square sum of the subgrid turbulent velocity dispersion within the GMC and the resolved nonthermal velocity dispersion. The subgrid turbulent velocity dispersion is calculated from the external pressure from the hot ISM (Robertson et al. 2004) using  $\sigma^2 = P/\rho_{\text{cell}}$  though we impose a ceiling of  $10 \text{ km s}^{-1}$  which comes from average values found in turbulent feedback simulations (e.g. Dib et al. 2006; Joung et al. 2009; Ostriker & Shetty 2011). The resolved nonthermal component is calculated by finding the turbulent velocity dispersion of the nearest neighbouring cells in the simulation. In detail, we calculate the standard deviation of the velocities of the nearest neighbour cells in the  $\hat{x}$ ,  $\hat{y}$  and  $\hat{z}$  directions, and define the nonthermal velocity dispersion as the mean of these. In cases where the GMC is unresolved, a floor  $\sigma_{\text{vir}}$  is set by assuming the cloud is in virial balance with a virial parameter  $\alpha_{\text{vir}} = 1$ , for  $\alpha_{\text{vir}} \equiv 5\sigma_{\text{vir}}^2 R/(GM)$ , so that

$$\sigma_{\text{vir}} = 2.2 \text{ km s}^{-1} \left[ \frac{M}{10^5 \text{ M}_{\odot}} \right]^{1/4} \quad (7)$$

for  $\Sigma_{\text{cloud}} = 100 \text{ M}_{\odot} \text{pc}^{-2}$  where  $M$  is the mass of the cloud.

Finally, we calculate the temperature of the model GMCs. The model is based on that developed by Krumholz et al. (2011), and we describe the relevant details here as it is an important aspect of our model. The temperature of the molecular ISM is determined by a balance of heating and cooling processes in the gas, heating and cooling of the dust, and a dust-gas thermal exchange. For the gas, we consider grain photoelectric heating at a rate per H nucleus  $\Gamma_{\text{pe}}$ , cosmic ray heating at a rate  $\Gamma_{\text{CR}}$ , and cooling via either CII or CO line cooling at a rate  $\Lambda_{\text{line}}$ . The dust can be heated by the background infrared radiation field at a rate  $\Gamma_{\text{dust}}$ , and cool via thermal emission at a rate  $\Lambda_{\text{dust}}$ . Finally, there is an energy exchange between dust and gas at a rate  $\Psi_{\text{gd}}$  where  $\Psi_{\text{gd}}$  is positive if the dust is hotter than the gas. If the gas and dust are in thermal balance, then we have the following equations:

$$\Gamma_{\text{pe}} + \Gamma_{\text{CR}} - \Lambda_{\text{line}} + \Psi_{\text{gd}} = 0 \quad (8)$$

$$\Gamma_{\text{dust}} - \Lambda_{\text{dust}} - \Psi_{\text{gd}} = 0 \quad (9)$$

The equation is solved by simultaneously iterating on the temperatures of the gas and dust<sup>6</sup>.

The grain photoelectric heating rate is assumed to be attenuated by half the mean extinction of the cloud (as the heating rate is expected to decrease toward the cloud interiors) and is given by:

$$\Gamma_{\text{pe}} = 4 \times 10^{-26} G'_0 e^{-N_{\text{H}}\sigma_d/2} \text{erg s}^{-1} \quad (10)$$

where  $G'_0$  is the FUV intensity relative to the Solar neighborhood, and  $\sigma_d$  is the dust cross section per H atom to UV photons. Here, we assume that the  $G'_0 = 1$  and  $\sigma_d = 1 \times 10^{-21} \text{ cm}^2$ . Test models in which we scale  $G_0$  by the star formation rate density compared to that found in the solar neighbourhood (e.g. Ostriker et al. 2010) have similar results to those presented in this work, and are presented in the Appendix.

The cosmic ray heating rate is given by:

$$\Gamma_{\text{CR}} = \zeta' q_{\text{CR}} \text{ s}^{-1} \quad (11)$$

<sup>6</sup> We note that this dust temperature is not always the same as the temperature calculated by SUNRISE (§ 2.3). This makes little difference on the final results. We discuss this in more detail in the Appendix.

where  $\zeta'$  is the cosmic ray ionisation rate (here, assumed to be  $2 \times 10^{-17} \text{ Z}' \text{ s}^{-1}$ ), and  $q_{\text{CR}}$  is the thermal energy increase per cosmic ray ionisation. For  $\text{H}_2$ ,  $q_{\text{CR}} \approx 12.25 \text{ eV}$  (though note that this value is quite uncertain; see discussion in Appendix A4 of Krumholz et al. 2011), and for HI,  $q_{\text{CR}} = 6.5 \text{ eV}$  (Dalgarno & McCray 1972). We utilise a constant cosmic ray heating rate for all simulations. Some models suggest that there may be enhanced cosmic ray fluxes during starbursts which would increase the  $\text{H}_2$  gas temperature (Papadopoulos 2010; Papadopoulos et al. 2010), and further enhance the effects found in our Results section.

Finally, in a subset of models we have explored the potential effects of turbulent heating on molecular clouds. In unresolved GMCs we can estimate this heating rate based on numerical experiments on the rate of turbulent dissipation:  $\Gamma_{\text{turb}} \approx 1.5 \times \sigma^3/R$ , where  $R$  is the GMC radius (McKee & Ostriker 2007). For resolved GMCs, we can measure the turbulent heating rate directly from the code. Bulk turbulent motions can be converted to heat through two pathways: adiabatic compression and viscous dissipation. The compressive heating rate per unit mass is  $\Gamma_{\text{comp}} = P(\nabla \cdot \mathbf{v})/\rho$ , and we can evaluate this directly from the density and velocity fields output by Gadget. The viscous dissipation rate per unit mass is  $\Gamma_{\text{visc}} = (\pi_{\text{visc}} \cdot \nabla) \cdot \mathbf{v}/\rho$ , where  $\pi_{\text{visc}}$  is the viscous stress tensor. The code relies on implicit dissipation rather than an explicit viscosity, but we can estimate the viscous heating rate produced by that implicit dissipation by noting that the Reynolds number must be  $\sim 1$  on the resolution scale of the code (Offner et al. 2009). This implies that the dynamic viscosity is  $\eta \approx \rho v h$ , where  $h$  is the SPH smoothing scale. Given this approximation, the components of the viscous stress tensor are  $\pi_{ij,\text{visc}} = \eta[\partial v_i/\partial x_j + \partial v_j/\partial x_i - (2/3)\partial v_i/\partial x_j \delta_{ij}]$ , and which we can again evaluate directly from the density and velocity fields output by Gadget. We find that the effects of turbulent heating are modest in both the resolved and unresolved cases. In our fiducial merger including viscous dissipation reduces  $X_{\text{CO}}$  by  $\sim 30\%$ , while the the fiducial disc it reduces  $X_{\text{CO}}$  by less than a few percent. Hereafter we neglect this heating term, though we note that including it would only enhance the results we present below.

The line cooling is assumed to occur via either CII or CO emission. The fraction of hydrogen for which the carbon is mostly in the form of CO is well-approximated by the following result from both semi-analytic (Wolfire et al. 2010) and numerical (Glover & Mac Low 2011) work:

$$f_{\text{CO}} = f_{\text{H}_2} \times e^{-4(0.53 - 0.045 \ln \frac{G'_0}{n_{\text{H}}/\text{cm}^{-3}} - 0.097 \ln Z')/A_V} \quad (12)$$

When this fraction is above 50%, we assume the cooling happens predominantly via CO line cooling; else, the cooling occurs via CII emission. The cooling rate is calculated via an escape probability formalism utilising the public code of Krumholz & Thompson (2007). We describe the equations for the line radiative transfer (both within clouds, as is pertinent to calculating the cooling rates, and across the model galaxy, in § 2.4).

The dust cooling rate is:

$$\Lambda_{\text{dust}} = \kappa(T_{\text{d}})\mu_{\text{H}}caT_{\text{d}}^4. \quad (13)$$

We assume the bulk of the dust heating happens via IR radiation as IR radiation likely dominates the heating over UV flux in the optically thick centres of GMCs. The IR radiation field is known from SUNRISE dust radiative transfer calculations (which will be described in § 2.3).

Finally, the dust and gas exchange energy via:

$$\Psi_{\text{gd}} = \alpha_{\text{gd}} n_{\text{H}} T_{\text{g}}^{1/2} (T_{\text{d}} - T_{\text{g}}) \quad (14)$$

where the thermal gas-dust exchange rate is  $\alpha_{\text{gd}} = 3.2 \times 10^{-34} \text{ Z}' \text{ erg cm}^3 \text{ K}^{-3/2}$  for  $\text{H}_2$ , and  $\alpha_{\text{gd}} = 1 \times 10^{-33} \text{ Z}' \text{ erg cm}^3 \text{ K}^{-3/2}$  for HI (Goldsmith 2001).

### 2.3 Dust Radiative Transfer

In order to calculate the background radiation field from stars and the dust temperature, we perform dust radiative transfer calculations with the publicly available code SUNRISE. A full description of the algorithms can be found in Jonsson (2006); Jonsson et al. (2010), and Jonsson & Primack (2010). Here, we summarise the aspects of the simulations most relevant to this study.

The sources of radiation in the model galaxies are stellar clusters and accreting black holes. The stellar clusters emit a template spectrum derived from STARBURST99 calculations, with the metallicities, masses and ages known from the GADGET-3 simulations. The AGN emits a spectrum based on observations of unreddened quasars (Hopkins et al. 2007b), though has little effect in the calculations here (see the Appendix).

The substructure of the ISM on scales below the smoothing length of the SPH simulations is unresolved. We assume that star clusters with ages  $< 10 \text{ Myr}$  reside in natal birthclouds, and modulate their SED accordingly. These birthclouds contain HII regions and photodissociation regions (PDRs) whose SEDs are calculated utilising 1D MAPPINGSIII photoionisation models (Groves et al. 2004, 2008; Jonsson et al. 2010). The time-averaged PDR covering fraction is a free-parameter. We assume a constant fraction of  $f_{\text{PDR}} = 0.3$ , corresponding to a covering lifetime of  $\sim 2 - 3 \text{ Myr}$  (Groves et al. 2008). This value is motivated in part by simulations by Jonsson et al. (2010) which showed covering fractions comparable to these result in synthetic SEDs of disc galaxies comparable to the SINGS sample (Kennicutt et al. 2003). Changing this parameter has minimal effects on the final results of this paper: we quantify this and other potential effects of the subresolution modeling in the Appendix.

When radiation leaves either the naked stellar cluster (with age  $> 10 \text{ Myr}$ ), or the HII region/PDR (for younger clusters), it is allowed to interact with the diffuse ISM. We assume the remaining cold molecular phase has an negligible cross-section for interaction, though test the effects of this assumption in the Appendix.

The dust mass in the diffuse ISM is calculated assuming a constant dust to metals ratio of 0.4 (Dwek 1998; Vladilo 1998; Calura et al. 2008), where the metallicity distribution is known from the SPH calculations. We use the Weingartner & Draine (2001) dust model with  $R \equiv A_V/E_{B-V} = 3.15$ , as updated by Draine & Li (2007). The dust and radiation field are assumed to be in radiative equilibrium, utilising the methodology of Juvela (2005) for calculating the converged radiation field. When the radiation field has converged, we calculate the dust temperature in each cell by iterating equations 6-8 of Jonsson & Primack (2010) utilising a Newton-Raphson scheme.

### 2.4 Molecular Line Radiative Transfer

Finally, with information about the spatial distribution of GMCs in the model galaxies, and their mean  $\text{H}_2$  fractions, densities, temperatures, velocity dispersions and kinematics through the galaxy, we are prepared to calculate the emergent CO line emission from the model galaxy. This involves two stages. First, we calculate the escape probabilities of the CO lines from the GMCs. We then track the propagation of these photons through the model galaxy as they potentially interact with other GMCs.

Generally, CO line emission is set by the level populations. The source function from a given region for a given transition from upper level to lower level  $u \rightarrow l$  is given by:

$$S_\nu = \frac{n_u A_{ul}}{(n_l B_{lu} - n_u B_{ul})} \quad (15)$$

where  $A_{ul}$ ,  $B_{lu}$  and  $B_{ul}$  are the Einstein coefficients for spontaneous emission, absorption, and stimulated emission, respectively, and  $n$  are the absolute level populations.

We first calculate the level populations within and probability for photons to escape from the individual GMCs in the galaxy utilising the publicly available code described in Krumholz & Thompson (2007). The levels are assumed to be in statistical equilibrium and determined through the rate equations:

$$\sum_l (C_{lu} + \beta_{lu} A_{lu}) f_l = \left[ \sum_u (C_{ul} + \beta_{ul} A_{ul}) \right] f_u \quad (16)$$

$$\sum_i f_i = 1 \quad (17)$$

where  $C$  are the collisional rates,  $f$  the fractional level populations, and  $\beta_{ul}$  is the escape probability for transition  $u \rightarrow l$ . The rate equations can be rearranged as an eigenvalue problem, and solved accordingly.

The escape probability,  $\beta_{ul}$  can be approximated by relating it to the optical depth in the line,  $\tau_{ul}$  (Krumholz & Thompson 2007):

$$\beta_{ul} \approx \frac{1}{1 + 0.5\tau_{ul}} \quad (18)$$

In the escape probability formalism, the optical depth of the line through the cloud can be represented as:

$$\tau_{ul} = \frac{g_l}{g_u} \frac{3A_{ul}\lambda_{ul}^3}{16(2\pi)^{3/2}\sigma} Q_{N_{H_2}} f_l \left( 1 - \frac{f_u g_l}{f_l g_u} \right) \quad (19)$$

where  $Q$  is the abundance of CO with respect to  $H_2$ ,  $g_l$  and  $g_u$  are the statistical weights of the levels,  $N_{H_2}$  is the column density of  $H_2$  through the cloud,  $\lambda_{ul}$  is the wavelength of the transition, and  $\sigma$  is the velocity dispersion in the cloud. Equations 16-19 are iterated upon utilising the Newton-Raphson Method until the escape probabilities and level populations within the GMCs are known.

With  $\beta_{ul}$  calculated, we determine the effects of radiation from individual GMCs on other GMCs in determining the final level populations utilising the 3D non-LTE Monte Carlo radiative transfer code TURTLEBEACH (Narayanan et al. 2006b, 2008b). We begin with the level populations found from the escape probability calculations as a guess, and emit model photons from each GMC isotropically with direction drawn randomly, and emission frequency drawn from a Gaussian profile function:

$$\phi(\nu) = \frac{1}{\Delta\nu_D \sqrt{\pi}} \exp \left\{ - \left( \nu - \nu_0 - \mathbf{v} \cdot \hat{\mathbf{n}} \frac{\nu_{ul}}{c} \right)^2 / \Delta\nu_D^2 \right\} \quad (20)$$

where  $\nu_0$  is the rest frequency of the line,  $v$  is the velocity of the cloud in the direction of the photon's emission,  $c$  is the speed of light, and  $\Delta\nu_D$  is the doppler-width of the emission line.

When the photon passes through a cell, it interacts with a GMC and sees an opacity of:

$$\alpha_\nu^{ul}(\text{gas}) = V_{\text{fill}} \left[ \frac{h\nu_{ul}}{4\pi} \phi(\nu) (n_l B_{lu} - n_u B_{ul}) \right] \quad (21)$$

where  $V_{\text{fill}}$  is the volume filling factor of the spherical GMC. We neglect absorption by dust in this model.

After all GMCs have emitted some number of model photons, the level populations in the GMCs are updated by assuming detailed balance:

$$n_l \left[ \sum_{k < l} \beta_{lk} A_{lk} + \sum_{k \neq l} (B_{lk} J_\nu + C_{lk}) \right] = \sum_{k > l} n_k \beta_{kl} A_{kl} + \sum_{k \neq l} n_k (B_{kl} J_\nu + C_{kl}) \quad (22)$$

where  $C_{lk}$  and  $C_{kl}$  are the collisional rates, and  $\beta$  only exists for transition  $k \rightarrow l$  such that  $k = l + 1$ . Equations 22 are solved via Gauss-Jordan matrix inversion.

This process is iterated upon until the level populations have achieved convergence. Here, we demand that they not vary by more than a fractional difference of  $1 \times 10^{-3}$  for at least 3 iterations.

Once the level populations have been solved for, we build the formal spectrum by choosing an (arbitrary) viewing angle, and integrating along lines of sight (e.g. Walker et al. 1994):

$$I_\nu = \sum_{z_0}^z S_\nu(z) [1 - e^{-\tau_\nu(z)}] e^{-\tau_\nu(\text{tot})} \quad (23)$$

Tests of TURTLEBEACH against the publicly available Leiden Benchmarks (van Zadelhoff et al. 2002) are presented in Narayanan et al. (2006b). We obtained our coefficients from the *Leiden Atomic and Molecular Database* (Schöier et al. 2005). We assume a fractional carbon abundance of  $1.5 \times 10^{-4}$ , though the abundance of CO with respect to  $H_2$  is given by Equation 12.

### 3 OBSERVATIONAL AND PHYSICAL PROPERTIES OF SIMULATED GALAXIES

As we aim to compare potential variations in  $X_{\text{CO}}$  in our simulated galaxy mergers to those that are actually observed, it is worth briefly comparing the physical and synthetic observational properties of our model galaxies to real galaxies. Our fiducial merger has been well-studied in the literature, and is very much an average merger simulation as far as the range of simulated SFRs, black hole accretion rates and bolometric luminosities. While the processes described in this section generically describe gas-rich mergers, what we summarise here has been calculated and published previously explicitly for our fiducial model.

The merger goes through elevated star formation rate upon first passage as tidal torques on the gas cause the gas to lose angular momentum and fall toward the centres causing high-density regions (Mihos & Hernquist 1996; Hopkins et al. 2006; Narayanan et al. 2008c; Juneau et al. 2009). The galaxy undergoes a starburst upon final coalescence, and peaks in its bolometric luminosity. Radiative transfer post-processing on these models have found that the model galaxy is then visible as a ULIRG (Chakrabarti et al. 2007). The same gaseous inflows can drive sufficient black hole growth to result in optical quasar activity (Di Matteo et al. 2005; Hopkins et al. 2005b,a, 2006). Effects of the AGN feedback can be seen in both the warm infrared colours of the galaxy (Younger et al. 2009), as well as molecular outflows (Narayanan et al. 2006a, 2008b).

The truncation of the starburst by a combination of gas consumption and AGN feedback can render the galaxy observable as an E+A post-starburst (Snyder et al. 2011) before it evolves into a dead early-type (Springel et al. 2005a; Hopkins et al. 2007a) with colours comparable to those observed on the red-sequence (Springel et al. 2005a; Hopkins et al. 2008b,c). The kinematic (Cox

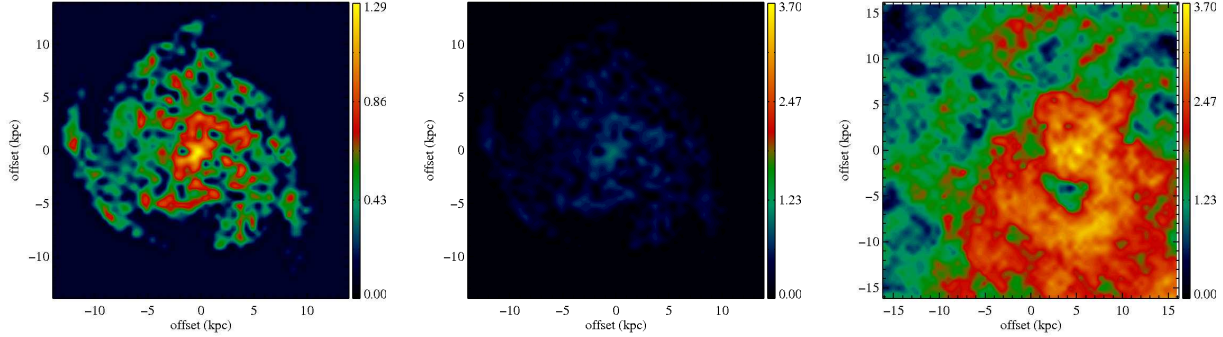


**Figure 1.** Velocity integrated brightness temperature  $W_{\text{CO}}$  maps for model disc galaxy (left), and fiducial merger snapshot (right). The colour scales correspond to the colour bars on the right of each panel, and the units are  $\log_{10} (\text{K-km s}^{-1})$ . The centre panel shows the model disc again, but with the same colour scale as the merger for comparison. Low gas kinetic temperature ( $\sim 10$  K) and velocity dispersions cause the bulk of the disc galaxy to have intensities of  $\sim 10$   $\text{K-km s}^{-1}$ . In contrast, the velocity dispersion within GMCs in the ULIRG can be many tens of  $\text{km s}^{-1}$ , with gas kinetic temperatures near 50 K. Summed over a sightline, the observed gas intensity can be  $> 10^3 \text{K-km s}^{-1}$ .

et al. 2006c), X-ray (Cox et al. 2006a), nuclear emission (Hopkins et al. 2008d, 2009), and molecular disc properties (Xu et al. 2010) of this merger remnant have all been studied and found to be comparable to those observed. Similarly, the remnant lies on the fundamental plane (Di Matteo et al. 2005; Robertson et al. 2006; Hopkins et al. 2008a).

## 4 RESULTS

### 4.1 GMCs in “Normal” Discs

In the far left panel of Figure 1, we show the velocity-integrated brightness temperature map of the model disc galaxy. As expected, the central regions are the brightest, and the outer disc has little CO emission. In the top left panel of Figure 2, we plot the emission-weighted distribution of  $X_{\text{CO}}$  values for the GMCs in our model disc galaxy and the fiducial model merger. We additionally plot the distribution of GMC physical properties in both the disc and merger. We will return to this plot frequently throughout this section and the next.

The luminosity-weighted  $X_{\text{CO}}$  in our model disc is  $\sim 4 \times 10^{20} \text{cm}^{-2}/\text{K-km s}^{-1}$  with a relatively narrow dispersion. The dispersion is narrow because the surface densities, kinetic temperatures and velocity dispersions of the model disc GMCs show fairly little variation. To remind the reader, the column densities in the GMCs in our disc galaxy are set to be the surface density of cold gas in the cell. When the GMC is unresolved in the simulation, we set the subgrid value of the surface density to  $\Sigma_{\text{cloud}} = 100 \text{M}_{\odot}/\text{pc}^2$ . This value was chosen to match the roughly constant surface density of Galactic molecular clouds. Nearly all of the GMCs in the model disc take on this value for a surface density.

The kinetic temperatures of GMCs in the disc have a relatively tight distribution near 10 K, as shown in Figure 2. Because the GMCs have a relatively low density compared with starbursts (the mass-weighted value is  $\sim 500 \text{cm}^{-3}$ ), there is little coupling with the dust grains (which are a factor of a few hotter; Figure 2). Thus the temperature is primarily determined by molecular line cooling, and heating by cosmic rays and the grain photoelectric effect. The kinetic temperature helps to set the brightness temperature, though the two are not identical. The emission-weighted brightness temperature for the merger(disc) are  $\sim 50(7)\text{K}$ .

Finally, the distribution of velocity dispersions in the GMCs is fairly narrow. Recalling § 2, the velocity dispersion of the clouds is taken by calculating the dispersion amongst the cell’s nearest neighbours, with a subgrid model for unresolved clouds (Equation 7). Because the disc is dynamically cold, the velocity dispersions are primarily set by the latter case. This results in an emission-weighted velocity dispersion within GMCs in the model disc of  $\sim 3 \text{km s}^{-1}$ , with a maximum of  $\sim 15 \text{km s}^{-1}$ . These values compare favourably with the velocity dispersions reported in the comprehensive survey of Solomon et al. (1987), and the more recent review by Blitz et al. (2007).

We can ask why the simulated  $X_{\text{CO}}$  from the model galaxy is comparable to the Galactic average,  $X_{\text{CO}} \approx 2 - 4 \times 10^{20} \text{cm}^{-2}/\text{K-km s}^{-1}$ . In principle this occurs because the physical conditions in the model GMCs by and large match those of observed GMCs in the Milky Way. In this sense, the fact that our model value for  $X_{\text{CO}}$  in quiescent discs matches that of the Galaxy is by construction. However, there are two salient points here.

First, it is important to remember that we allow for the possibility that the galactic environment can set the physical conditions in the GMCs if the pressure is sufficiently high. The fact that the default value for the surface density and velocity dispersions in the clouds is typically used is a statement that the galactic environment in the model disc galaxy is not sufficiently extreme to cause significant changes in the surface densities, temperatures, or velocity dispersions in the GMCs from the Galactic values. As we will see in the subsequent section, this is not the case in mergers.

Second, the subresolution values for the GMCs are not without physics. GMCs through the Local Group are observed to obey the Larson (1981) relations: they follow a linewidth-size relationship with  $\sigma \propto R^{0.5}$ , they have virial parameters  $\alpha \sim 1$ , and they all have roughly the same surface density  $\Sigma \sim 100 \text{M}_{\odot} \text{pc}^{-2}$  (Blitz et al. 2007; Bolatto et al. 2008). The origin of these observed relationships is debated, but their universality argues for some sort of internal regulation mechanism operating in GMCs (e.g. Krumholz et al. 2006; Shetty & Ostriker 2008). Regardless of the underlying mechanism, though, our subgrid model is not simply tuned to reproduce the “right”  $X_{\text{CO}}$ . Instead, it models the real physical properties of GMCs<sup>7</sup>.

<sup>7</sup> We note, however, that clouds need not be virialised to have  $X_{\text{CO}}$  com-

Finally, it is important to note that the results presented in this section do not necessarily translate to disc galaxies at high-redshift. Galaxies on the “main-sequence” of star formation rates at high- $z$  (e.g. Noeske et al. 2007a,b) still form stars at rates comparable to present-epoch mergers (Daddi et al. 2005, 2007) because they have very high gaseous surface densities, though they may be morphologically classified as discs (Förster Schreiber et al. 2009).

#### 4.2 $X_{\text{CO}}$ in Merger-Driven Starbursts

We now turn to  $X_{\text{CO}}$  in galaxy mergers. Before embarking on the remainder of this section, it is important to emphasise that the many of the GMCs in the model starburst are resolved (this is clear from the  $\Sigma_{\text{H}_2}$  panel in Figure 2). Thus, the derived values for  $X_{\text{CO}}$  are independent of subresolution assumptions.

During the merger, gas is funneled toward the nuclear regions, causing dense concentrations of molecular gas (Barnes & Hernquist 1991, 1996). The surface densities of the GMCs in our simulations rise accordingly. In principle, this would cause a rise in the CO- $\text{H}_2$  conversion factor (c.f. Equation 2). However, during the merger-induced starburst, the increase in velocity-integrated line intensity exceeds the rise in surface density, causing  $X_{\text{CO}}$  to drop from the Galactic value.

In Figure 3, we show the evolution of the star formation rate, gas temperature, velocity dispersion and  $X_{\text{CO}}$  as a function of time for the three model galaxy mergers. The shaded region denotes the range of mean values among the GMCs within the merger models at each timestep, i.e. at time 0 the lowest point outlined in gray corresponds to the lowest galaxy-averaged value of the three merger models, and the highest point in gray corresponds to the highest galaxy-averaged value among the three. The time axes are centred around the peak in the starburst for each model. When the galaxies merge, the discs are destroyed. During this time, the dominant contributor to  $\sigma$  within the GMCs is the nonthermal component derived from the local resolved velocity dispersion of the gas. The nonthermal velocity dispersion is driven by the dynamics during the galaxy merger and mixing of stellar mass with the  $\text{H}_2$  gas.

During final coalescence in the merger, when the SFR peaks at a few hundred  $\text{M}_{\odot}\text{yr}^{-1}$ , the fraction of dense gas rises, a result verified both in theoretical models (e.g. Mihos & Hernquist 1994, 1996; Narayanan et al. 2008a,c; Bournaud et al. 2011), and observations (Juneau et al. 2009). The mass-weighted mean GMC density rises to roughly  $\gtrsim 10^4 \text{ cm}^{-3}$ , compared to  $\sim 500 \text{ cm}^{-3}$  in the model disc. At these high densities, the energy exchange between dust and gas becomes efficient, and the gas temperatures begin to approach the dust temperatures. At the same time, the dust is being heated by an amplified radiation field due to the merger-induced starburst. This is demonstrated explicitly in Figure 2, where we show the dust and gas (kinetic) temperature distributions of the GMCs in the model galaxies. The mean gas temperature is higher by a factor of a few than the roughly  $\sim 10 \text{ K}$  GMCs in the model disc. The rise in the gas kinetic temperature during the starburst is shown in Figure 3 as well<sup>8</sup>.

parable to observed galactic values. Provided that  $\Sigma_{\text{cloud}}$ ,  $T$ , and  $\sigma$  remain within a modest range of values,  $X_{\text{CO}} \sim 2 - 4 \times 10^{20} \text{ cm}^{-2}/\text{K-km s}^{-1}$  (Shetty et al. 2011b).

<sup>8</sup> We remind the reader that we adopt a constant cosmic ray ionisation rate in all models. If cosmic ray energy densities increase in starburst environments as suggested by recent observational (Abdo et al. 2010a) and theoretical (Papadopoulos 2010; Papadopoulos et al. 2010) work, then the gas temperatures would further increase, causing  $X_{\text{CO}}$  in starbursts to fall

The large molecular gas densities in the merger also mean the CO is thermalised in the ground state transition. When level populations are in local thermodynamic equilibrium (LTE), their source function can be described by the Planck Function. In this limit, the source function rises with temperature. Hence, the rise in gas kinetic temperature during the burst contributes to driving  $X_{\text{CO}}$  down.

The combination of the increased velocity dispersion and the brightness temperature combine to exceed the increase in surface density, which causes a depressed mean  $X_{\text{CO}}$  from the Galactic value during the merger. We now return to the first panel Figure 2 to explicitly compare  $X_{\text{CO}}$  in the merger against the disc galaxy. We see that  $X_{\text{CO}}$  has a broad distribution for the model merger. A number of GMCs outside of the nucleus are similar to the disc galaxy’s in terms of their physical properties. These GMCs are unresolved in our simulations (owing to the fact that they reside in lower-density environments), and thus take on surface density and velocity dispersion values comparable to those observed in the Galaxy. However, the GMCs toward the centre of the galaxy all have larger surface densities, velocity dispersions, and kinetic temperatures. The latter two combine to depress  $X_{\text{CO}}$  compared to the values seen in the disc by a factor of  $\sim 5 - 10$ . Because most of the mass in the merger is in the central regions, the luminosity-weighted mean is low. Test simulations with fixed temperatures or velocity dispersions show that the increased kinetic temperature and velocity dispersion in the gas contribute roughly equally to the increased line intensity in the merger simulation. This is somewhat apparent from Figure 2, where we see similar distributions values for the kinetic temperatures and velocity dispersions in the gas.

The magnitude by which  $X_{\text{CO}}$  decreases is dependent on the strength of the merger. Turning to Figure 3, we see a range in  $X_{\text{CO}}$  values during the burst. The model with the largest  $X_{\text{CO}}$  during the burst corresponds to the lowest peak SFR. A key point of this aspect of the model is that there is no “merger value” of  $X_{\text{CO}}$ :  $X_{\text{CO}}$  depends on the physical parameters of the emitting galaxy.

What happens in the post-starburst stage is also highly merger-specific. During this phase, the galaxy is a gas-poor early type. Generally, the gas has a large velocity dispersion for at least a dynamical time after the burst. This is consistent with what was seen in simulations of CO gas in high- $z$  submillimetre galaxies (Narayanan et al. 2009). During this phase, it is less trivial to simply relate the observed  $X_{\text{CO}}$  to the gas velocity dispersion and temperature as there is a much larger dispersion in molecular gas fractions and CO abundances. This owes to the fact that there are highly varying physical conditions in the post-burst galaxy, which drive strong variations in the  $\text{H}_2$  and CO abundances. Some of the simulations return to a Galactic  $X_{\text{CO}}$  value quickly, while others remain low.

In summary, during the merger-induced starburst,  $X_{\text{CO}}$  drops in galaxies from the standard Galactic value due to increased gas temperatures and velocity dispersions. During this time, the CO abundances are  $\sim 1 \times 10^{-4}/\text{H}_2$  and molecular gas fractions near unity in the main CO emitting region. In the resulting gas-poor merger remnant, the dynamical and thermal history can vary from model to model, and the evolution of  $X_{\text{CO}}$  is less uniform among mergers.

even further (though see Bell et al. 2006, for an expanded study on the role of cosmic rays in the  $X$ -factor at various extinctions).



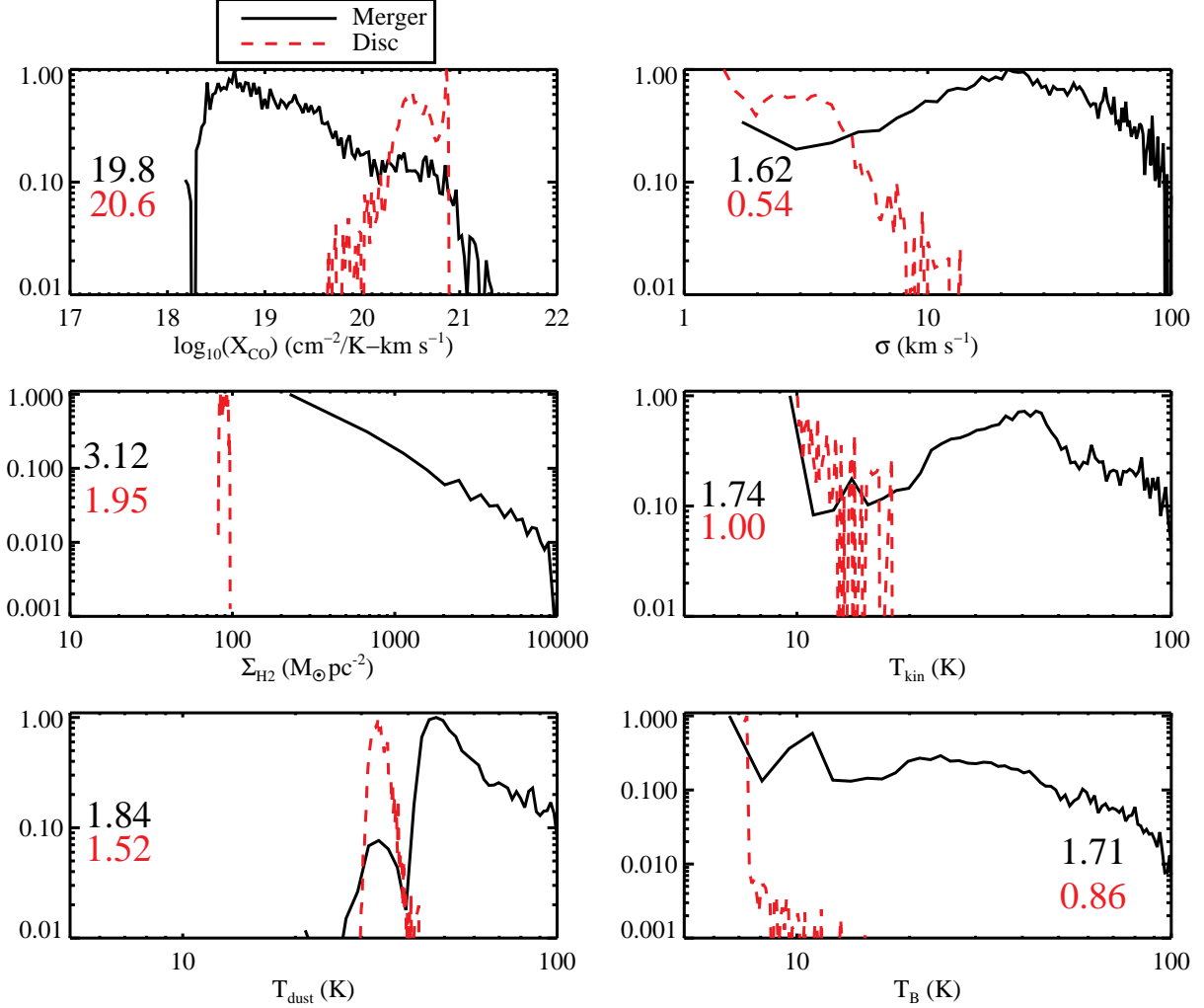


**Figure 2.** Emission-weighted distributions of  $X_{\text{CO}}$  values and physical properties for the GMCs in the model disc galaxy (red-dashed line) and fiducial merger model (solid-black line). The ordinate values are normalised. Starting from the top left, and going clock-wise, the plots show  $X_{\text{CO}}$ , velocity dispersion, kinetic temperature, brightness temperature, dust temperature, and GMC surface density. The disc galaxy predominantly has GMCs with physical properties comparable to the Milky Way's, and thus has similar  $X_{\text{CO}}$  values. The GMCs in the merger show a broad distribution in  $X_{\text{CO}}$  values, with a lower mean than the disc galaxy. The lower  $X_{\text{CO}}$  owes to larger gas temperatures (which are larger due to efficient coupling with the warm dust at high densities) and large velocity dispersions in the gas. The numbers in each panel refer to the  $\log_{10}$  of the emission-weighted mean value, and the black (top) number corresponds to the merger whilst the red (bottom) corresponds to the disc. Because the numbers correspond to the  $\log_{10}$  of the mean in the physical quantities, they will have larger values than one would pick by eye in the log-log plots.

### 4.3 The Variation of $X_{\text{CO}}$ with Galactocentric Radius

With the concepts presented in § 4.2, we are now in a position to understand how  $X_{\text{CO}}$  varies in galaxies as a function of spatial location. In Figure 4, we show the simulated  $X_{\text{CO}}$  maps for the disc galaxy and fiducial merger, and in Figure 5, we plot the values for  $X_{\text{CO}}$  in the GMCs in our model disc galaxy and fiducial merger as a function of radius from the centre of the galaxy. The  $X_{\text{CO}}$  values from Figure 5 come from the map in Figure 4. The  $X_{\text{CO}}$  values are binned in bins of distance, and represent the emission-weighted mean within a given distance bin. The bars denote the range of  $X_{\text{CO}}$  values seen in a given distance bin.

$X_{\text{CO}}$  in the centre of the model disc galaxy is systematically lower than in the rest of the galaxy. In particular, a number of GMCs along the line of sight have velocity dispersions larger than the typ-

ical virialised values, with values elevated by a factor of  $\sim 2$ . Similarly, due to the elevated densities in the nucleus combined with a warmer dust temperature, the gas temperatures of some GMCs can reach values up to 15 K. This causes  $X_{\text{CO}}$  in the central kiloparsec to generally display the lowest values in the galaxy. Depressed values of  $X_{\text{CO}}$  from the Galactic mean have been observed in at least a few GMCs toward the Galactic Centre (Oka et al. 1998). It is important to note that the regions where  $X_{\text{CO}} > 10^{21} \text{ cm}^{-2} / \text{K-km s}^{-1}$  represents much of the area, but a negligible fraction of the gas mass in the galaxy. This is evident from Figure 2.

In the fiducial model merger, unlike the situation with the model disc galaxy, we see no clear trend in  $X_{\text{CO}}$  with galactocentric radius. Due to the violent nature of the gasdynamics during the merger, gas of a variety of physical conditions is mixed

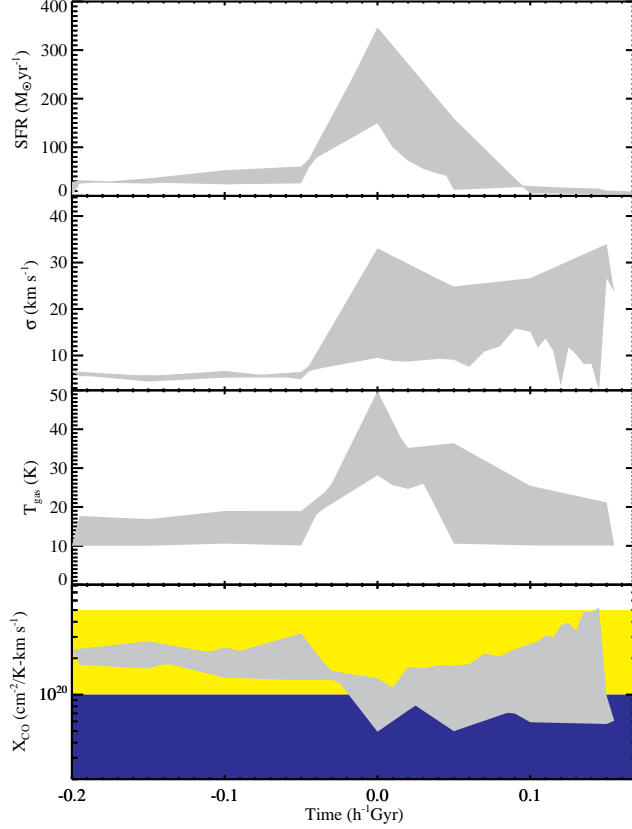


**Figure 3.** The evolution of the star formation rate, emission-weighted velocity dispersion, kinetic temperature, and  $X_{\text{CO}}$  of the individual GMCs within the galaxies for all three merger models as a function of time. The time axes are centred for each model about the point of maximum star formation rate. The grey shaded region denotes the range in emission-weighted mean values for all three models. This means that at a given time step, the shaded region is defined by the maximum and minimum value of a given quantity seen among the three merger models. In the bottom panel, the yellow and blue bands denote the typical ranges of  $X_{\text{CO}}$  observed for the Galaxy and ULIRGs, respectively (as compiled by Tacconi et al. 2008). Prior to the burst, the inspiralling discs have  $X_{\text{CO}}$  values comparable to the Galactic mean. Upon the merger, increased velocity dispersions and gas temperatures contribute to lowering  $X_{\text{CO}}$ . In the post-merger stage, differences in  $\text{H}_2$  abundances, CO abundances, and time for the gas to re-virialise contribute toward a large dispersion in  $X_{\text{CO}}$  values.

together. Consequently, we see a large range of  $X$ -factors in the GMCs throughout the galaxy.

Because the emission from the merger is irregular, it is possible that by choosing a different centre, the results from Figure 5 would change. To test this, we recentered the image on the peak of the velocity-integrated intensity. Doing this provides no substantial change in the results of Figure 5.

## 5 DISCUSSION

### 5.1 Observational Consequences of the Model

We have presented a model in which  $X_{\text{CO}}$  in GMCs is dependent on the physical conditions within the clouds. When the surface densities, kinetic temperatures and velocity dispersions within the GMCs resemble those of observed clouds in the Galaxy, the resulting  $X_{\text{CO}}$  factor is comparable to the observed Galactic mean value. In starbursts, while the surface densities of clouds are higher, this is offset by both larger velocity dispersions in the GMCs as well as larger gas temperatures. The increased linewidths represent the

turbulent velocity dispersion in the merger, as well as the stellar potential. The increased gas temperatures owe to efficient coupling with the dust at the high densities encountered in a merger. A fundamental point of this study is that the physical conditions which cause  $X_{\text{CO}}$  to vary in starbursts are coupled. The same processes which drive the increased gas surface density also cause an increase in star formation rate which drives up the dust and consequently the gas temperatures. Similarly, in a merger-driven burst, the gas velocity dispersion rises during the merger.

While it is of utmost importance to parameterise  $X_{\text{CO}}$  in terms of observable properties, because the physical parameters which drive observed values of  $X_{\text{CO}}$  are coupled, this is a nontrivial task which is outside the scope of this work (though it will be investigated in a forthcoming paper). Empirically, there is a tentative trend that  $X_{\text{CO}}$  decreases with increasing galaxy surface density (Tacconi et al. 2008). In the context of the models presented here, such a trend is plausible (see also Shetty et al. 2011b). One might expect that higher surface density systems typically arise in situations when the velocity dispersion is high and the star formation rates, dust temperatures and gas temperatures are also high.

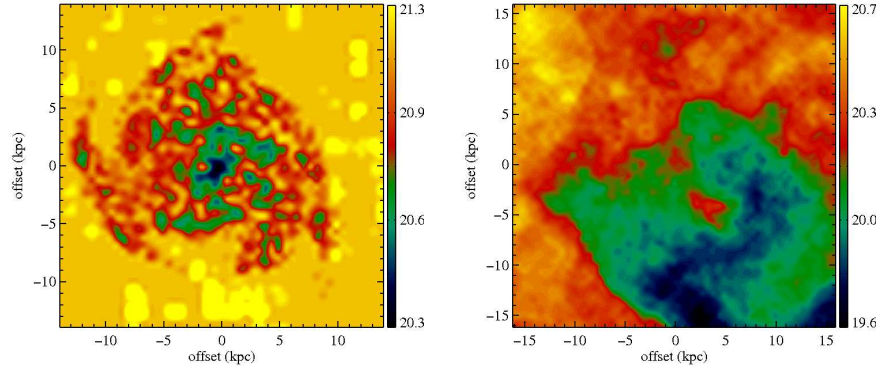


**Figure 4.** Maps of  $X_{\text{CO}}$  for the fiducial disc galaxy and merger. The colour scale denotes  $\log_{10} (\text{cm}^{-2}/\text{K-km s}^{-1})$ .  $X_{\text{CO}}$  is lower toward the centre of the disc galaxy due to higher temperatures and velocity dispersions in the clouds. The warm and high- $\sigma$  gas is somewhat more spread out in the merger. We enforce a maximum  $X_{\text{CO}}$  in the color bar of the disc galaxy of 21.3 to aid in clarity, though there are a few pixels with values as high as 21.8.

While the models investigated here by no means comprise an exhaustive parameter-space study of galaxy masses, merger mass ratios, or merger orbits, we can investigate whether  $X_{\text{CO}}$  can be parameterised by  $\Sigma_{\text{H}_2}$  in the simulations. To increase the dynamic range of surface densities in our models, we include one additional simulation of a high-redshift merger. The merger is the model submillimetre galaxy of Hayward et al. (2011) during the coalescence when the peak merger-induced starburst is  $\sim 4500 \text{ M}_{\odot} \text{yr}^{-1}$ . The model submillimetre galaxy has been shown to reproduce both the observed SED (Narayanan et al. 2010b), CO properties (Narayanan et al. 2009), overlap with  $24 \text{ } \mu\text{m}$  sources (Narayanan et al. 2010a), and number counts of observed SMGs (Hayward et al. 2010). Similarly, to increase the number of galaxies in our sample, we include many snapshots for the mergers (i.e. not just the snapshots at peak SFR).

We plot the emission-weighted mean  $X_{\text{CO}}$  of the GMCs in our model galaxies versus their emission-weighted mean surface densities in Figure 6. The models include the model mergers described in § 2, the model disc galaxy, and the newly introduced model submillimetre galaxy. The galaxies are binned by  $\Sigma_{\text{H}_2}$ . The trend seen is what is expected: that  $X_{\text{CO}}$  should decrease with gas surface density. In principle this owes to the fact that the highest surface density galaxies in our simulations are also forming stars at  $10^2 - 10^3 \text{ M}_{\odot} \text{yr}^{-1}$ , and have relatively large velocity dispersions. However, we emphasise strongly that Figure 6 is to be taken as a qualitative trend, rather than robust. A larger parameter-space survey of the simulations will be undertaken for a future study to identify the true mean and dispersions of  $X_{\text{CO}}$  as a function of  $\Sigma_{\text{H}_2}$ .

The variation in  $X_{\text{CO}}$  with environment may have implications for observed Kennicutt-Schmidt star formation laws. An example of this was presented by Daddi et al. (2010) and Genzel et al. (2010) who applied a starburst  $X_{\text{CO}}$  value to the inferred mergers in their observed sample of galaxies, and a Galactic  $X_{\text{CO}}$  value to the discs. Doing so results in a bimodal star formation rate surface density-gas surface density relation. On the other hand, Ostriker & Shetty (2011) pointed out that if a simple  $\Sigma$ -dependent

$X_{\text{CO}} \propto \Sigma^{-0.5}$  is used above  $\Sigma_{\text{H}_2} = 100 \text{ Msun/pc}^2$ , a unimodal empirical star formation relation results (with  $\Sigma_{\text{SFR}} \propto \Sigma^2$ , consistent with theoretical expectations for self-regulated star formation in this regime).

Interpreting results for high-redshift galaxies in the context of our model is complex. Our model advocates for lower  $X_{\text{CO}}$  values in high surface density environments. However, galaxies at  $z \sim 2$  which have surface densities comparable to local ULIRGs may in fact be discs (e.g. Daddi et al. 2005; Genzel et al. 2006; Förster Schreiber et al. 2009; Hopkins et al. 2010). How  $X_{\text{CO}}$  of high- $z$  discs should scale in this model is unclear at present. While their surface densities are comparable to local ULIRGs, their velocity dispersions may not show the same enhancement as seen in our model mergers. However, their gas temperatures may be comparable to their dust temperatures if the densities are high enough. Work by the Chicago group (R. Feldmann et al. in prep.) is underway to investigate this. Either way, the fact that our results tentatively suggest a relationship between  $X_{\text{CO}}$  and surface density implies a continuum in  $X_{\text{CO}}$  values, rather than a bimodality. Thus the relationship between our model results and the interpretation of high- $z$  observations by Daddi et al. (2010) and Genzel et al. (2010) will depend on the distribution of surface densities in their observed galaxies, among other issues. We note, however, that our work, like that of Teyssier et al. (2010), is consistent with the idea that the observed behaviour in the star formation rates and  $X_{\text{CO}}$  can be explained without the need to invoke a volumetric star formation law that is different in discs and mergers. The change in  $X_{\text{CO}}$  we see in our simulations occurs because of changes in the physical conditions of GMCs associated with the merger, and not because the underlying star formation law is different.

Finally, the concepts presented in this paper are testable in the near future with ALMA. Our models suggest that high spatial resolution observations of nearby ULIRGs will display both large velocity dispersions in the CO gas, and larger brightness temperatures than those seen in observations of Galactic GMCs on a comparable scale. We see this when comparing the panels of Figure 1. Some observational evidence for this already exists. Interferomet-

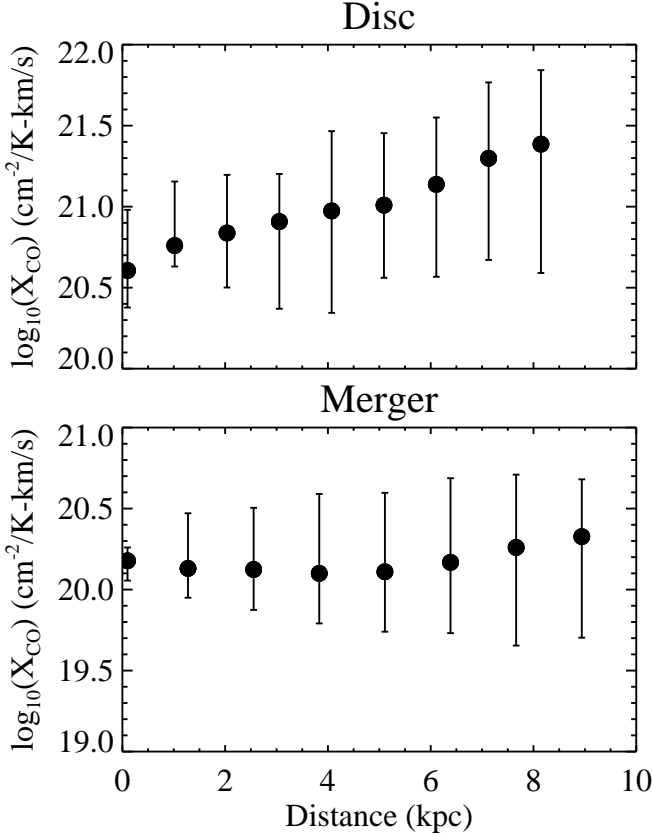


**Figure 5.**  $X_{\text{CO}}$  as a function of spatial distribution for the molecular gas in model disc (top) and merger (bottom). The  $X_{\text{CO}}$  is derived from the maps (Figure 4), and is the emission-weighted mean  $X_{\text{CO}}$  in bins of galactocentric distance. The bars around the points represent the range of  $X_{\text{CO}}$  values within a given distance bin. The molecular gas at the centre of the disc has systematically lower  $X_{\text{CO}}$  values than the outer disc. In the merger,  $X_{\text{CO}}$  shows a wide-range of values throughout the galaxy.

ric surveys of the central regions of nearby ULIRGs show velocity dispersions of hundreds of  $\text{km s}^{-1}$ , and brightness temperatures of tens of Kelvin (e.g. Scoville et al. 1997; Downes & Solomon 1998). Similarly, unresolved observations of starbursts have shown gas and dust temperatures in the range of 30–50 K, in agreement with the models presented here (Yao et al. 2003; Narayanan et al. 2005; Leech et al. 2010; Mao et al. 2010; Mühle et al. 2011).

## 5.2 Relationship to Other Models

The seminal work of Maloney & Black (1988) investigated  $X_{\text{CO}}$  in galaxies via subresolution models of GMCs in a disc-like configuration. These authors found that  $X_{\text{CO}}$  would vary from the Galactic value in cases of high kinetic temperature, high velocity dispersion or low metallicity. While not simultaneously modeling any of these effects, this model identified some of the most important driving factors in setting the observed  $X$ -factor in clouds.

A number of other studies have also investigated  $X_{\text{CO}}$  in models of giant molecular clouds. Early studies implemented 1D radiative transfer calculations in spherical models of GMCs (e.g. Kutner & Leung 1985; Wall 2007). With the increase of computational power, 3D numerical studies of GMCs in evolution have recently become feasible. Recently, Glover et al. (2010) and Glover & Mac

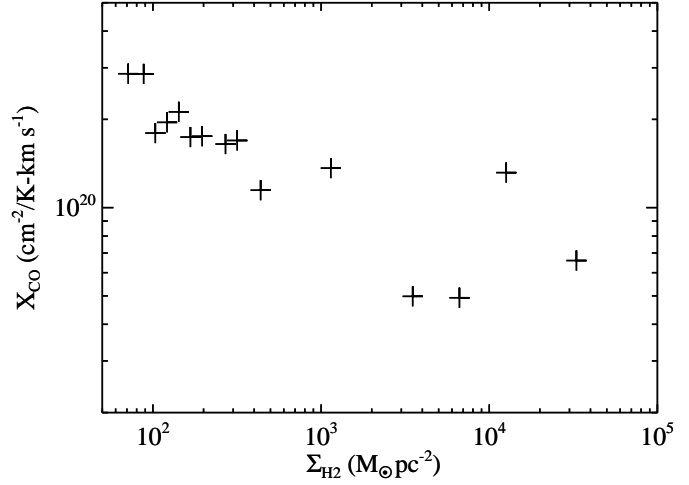


**Figure 6.** Emission-weighted mean  $X_{\text{CO}}$  in GMCs for each model galaxy versus their emission-weighted mean surface density. The points represent the mean values for all of the GMCs within individual galaxies, and the galaxies are binned by surface density. In order to increase our sample size, many snapshots (i.e. not just the peak SFR for the mergers), as well as a model submillimetre galaxy, were included in this plot. Higher surface density environments tend to correspond with merger-driven starbursts in our models, and hence larger values of  $\sigma$  and  $T_{\text{K}}$ . In these cases,  $X_{\text{CO}}$  tends to be lower than the standard Galactic value.

Low (2011) modeled  $\text{H}_2$  and CO formation/destruction in magnetohydrodynamic models of GMCs. These models were elaborated upon by Shetty et al. (2011a,b) who utilised radiative transfer calculations in combination with these MHD models to produce bona fide observables from the model clouds. These authors found that model GMC with mean densities, column densities, temperatures, and velocity dispersions comparable to the Milky Way’s clouds ( $n \sim 10^2 - 10^3 \text{ cm}^{-3}$ ,  $N_{\text{H}_2} \sim 10^{21} - 10^{22} \text{ cm}^{-2}$ ,  $T \sim 10 - 20 \text{ K}$ ,  $\sigma \sim 1 - 6 \text{ km s}^{-1}$ ) had average  $X_{\text{CO}}$  factors of order  $2 - 4 \times 10^{20} \text{ cm}^{-2}/\text{K-km s}^{-1}$ , and were insensitive to detailed temperature and velocity distributions. When manually increasing the velocity dispersion and/or temperature of the GMC, the resulting  $X_{\text{CO}}$  values fell by a factor of  $\sim 5$ , comparable to both observed starbursts and the model mergers in this paper. While the simulations in Shetty et al. do not model the physical processes which may simultaneously cause  $N_{\text{H}_2}$ ,  $\sigma$ , and  $T$  to vary, these models do confirm that when increasing  $\sigma$  or  $T$  and considering the radiative transfer through clouds, one will observe a depressed  $X_{\text{CO}}$ , as is inferred in ULIRGs.

In this sense, the models of Shetty et al. are complementary to those presented here. Shetty et al.’s models resolve much of the physics and chemistry within GMCs, though they have no information regarding the external environment from the host galaxy and how it may affect the cloud. Our simulations describe the ambient environment surrounding the model GMCs, though at best they resolve the surfaces of the clouds (and require some amount of subresolution techniques). That both sets of models are converging upon the same result from different directions is encouraging. The next step forward will be to fully couple galaxy evolution simulations with high-resolution models of GMCs with a grid of model GMCs. These efforts are underway and will be presented in due course (R. Feldmann et al. in prep; Narayanan & Shetty in prep.).

## 6 SUMMARY AND CONCLUSIONS

Utilising a combination of hydrodynamic simulations of disc galaxy evolution and galaxy mergers, dust and molecular line radiative transfer calculations, we investigated the dependence of the CO-H<sub>2</sub> conversion factor on galactic environment. Our main results follow:

(i) Provided that GMCs are gravitationally bound, disc galaxies in the local Universe have relatively little influence on the physical properties of GMCs within them (outside the central  $\sim$  kpc). The velocity dispersions are typically dominated by internal processes to the GMC, and the temperatures are roughly constant at  $\sim$  10 K, set by a balance of molecular/atomic line cooling and cosmic ray and grain photoelectric effect heating. In this situation, when the surface densities of GMCs are comparable to those in the Galaxy,  $X_{\text{CO}}$  will be similar to the Galactic value of  $X_{\text{CO}} \approx 2 - 4 \times 10^{20} \text{ cm}^{-2} \text{ K-km s}^{-1}$ .

(ii) In galaxy mergers, the GMC physical properties are strongly affected by the galaxy environment. The rise in surface density in GMCs during the merger is offset by an increase in the velocity dispersion coupled to a rise in the kinetic temperature of the gas caused by efficient dust-gas thermal exchange at high densities. The combination of increased velocity dispersion and kinetic temperature increases the CO intensity, and lowers the observed  $X_{\text{CO}}$  from the Galactic value by a typical factor of  $\sim 2 - 10$ .

(iii) There is a slight trend with galactocentric radius such that GMCs toward the centres of disc galaxies will have a lower  $X_{\text{CO}}$  than the disc-averaged value, owing to both increased velocity dispersions in the clouds, as well as higher kinetic temperatures.

## ACKNOWLEDGEMENTS

This work benefited from discussions had and coding done at the Aspen Center for Physics. DN would like thank Patrik Jonsson for numerous helpful conversations regarding adaptive mesh techniques in radiative transfer modeling, and Rahul Shetty, Andrew Baker, Emanuele Daddi, Robert Feldmann, Adam Leroy, Padelis Papadopoulos, and Erik Rosolowsky for sharing their knowledge on  $X_{\text{CO}}$  in galaxies. As always, T.J. Cox's wisdom was invaluable in understanding the physics associated with galaxy mergers. The authors thank the referee, Simon Glover, for a constructive report. Finally, DN would like to thank Rob Kennicutt for providing the original motivation to pursue this study following an insightful question at the 2007 Gas Accretion and Star Formation Workshop in Garching. DN acknowledges support from the NSF via grant AST-1009452. MK acknowledges support from: an Alfred P. Sloan Fellowship; the NSF through grants AST-0807739 and CAREER-0955300; and NASA through Astrophysics Theory and Fundamental Physics grant NNX09AK31G and a *Spitzer Space Telescope* Theoretical Research Program grant. ECO acknowledges support from the NSF via grant AST-0908185. The simulations in this paper were run on the Odyssey cluster, supported by the Harvard FAS Research Computing Group.

## References

Abdo, A. A. et al. 2010a, *ApJ*, 709, L152  
 —. 2010b, *ApJ*, 710, 133  
 Arimoto, N., Sofue, Y., & Tsujimoto, T. 1996, *PASJ*, 48, 275  
 Barnes, J. E. & Hernquist, L. 1996, *ApJ*, 471, 115

Barnes, J. E. & Hernquist, L. E. 1991, *ApJ*, 370, L65  
 Bell, T. A., Roueff, E., Viti, S., & Williams, D. A. 2006, *MNRAS*, 371, 1865  
 Bell, T. A., Viti, S., & Williams, D. A. 2007, *MNRAS*, 378, 983  
 Bigiel, F., Leroy, A., Walter, F., Brinks, E., de Blok, W. J. G., Madore, B., & Thornley, M. D. 2008, *AJ*, 136, 2846  
 Blitz, L., Fukui, Y., Kawamura, A., Leroy, A., Mizuno, N., & Rosolowsky, E. 2007, in *Protostars and Planets V*, ed. B. Reipurth, D. Jewitt, & K. Keil, 81–96  
 Blitz, L. & Rosolowsky, E. 2006, *ApJ*, 650, 933  
 Bloemen, J. B. G. M., Strong, A. W., Mayer-Hasselwander, H. A., Blitz, L., Cohen, R. S., Dame, T. M., Grabelsky, D. A., Thaddeus, P., Hermsen, W., & Lebrun, F. 1986, *A&A*, 154, 25  
 Bolatto, A. D., Leroy, A. K., Rosolowsky, E., Walter, F., & Blitz, L. 2008, *ApJ*, 686, 948  
 Boselli, A., Lequeux, J., & Gavazzi, G. 2002, *AP&SS*, 281, 127  
 Bouché, N. et al. 2007, *ApJ*, 671, 303  
 Bournaud, F., Chapon, D., Teyssier, R., Powell, L. C., Elmegreen, B. G., Elmegreen, D. M., Duc, P., Contini, T., Epinat, B., & Shapiro, K. L. 2011, *ApJ*, 730, 4  
 Calura, F., Pipino, A., & Matteucci, F. 2008, *A&A*, 479, 669  
 Chakrabarti, S., Cox, T. J., Hernquist, L., Hopkins, P. F., Robertson, B., & Di Matteo, T. 2007, *ApJ*, 658, 840  
 Cox, T. J., Di Matteo, T., Hernquist, L., Hopkins, P. F., Robertson, B., & Springel, V. 2006a, *ApJ*, 643, 692  
 Cox, T. J., Jonsson, P., Primack, J. R., & Somerville, R. S. 2006b, *MNRAS*, 373, 1013  
 Cox, T. J. et al. 2006c, *ApJ*, 650, 791  
 Daddi, E., Elbaz, D., Walter, F., Bournaud, F., Salmi, F., Carilli, C., Dannerbauer, H., Dickinson, M., Monaco, P., & Riechers, D. 2010, *ApJ*, 714, L118  
 Daddi, E. et al. 2005, *ApJ*, 631, L13  
 —. 2007, *ApJ*, 670, 156  
 Dalgarno, A. & McCray, R. A. 1972, *ARA&A*, 10, 375  
 Dame, T. M., Hartmann, D., & Thaddeus, P. 2001, *ApJ*, 547, 792  
 Di Matteo, T., Springel, V., & Hernquist, L. 2005, *Nature*, 433, 604  
 Dib, S., Bell, E., & Burkert, A. 2006, *ApJ*, 638, 797  
 Dickman, R. L. 1975, *ApJ*, 202, 50  
 Dobbs, C. L., Glover, S. C. O., Clark, P. C., & Klessen, R. S. 2008, *MNRAS*, 389, 1097  
 Downes, D. & Solomon, P. M. 1998, *ApJ*, 507, 615  
 —. 2003, *ApJ*, 582, 37  
 Draine, B. T., Dale, D. A., Bendo, G., Gordon, K. D., Smith, J. D. T., Armus, L., Engelbracht, C. W., Helou, G., Kennicutt, Jr., R. C., Li, A., Roussel, H., Walter, F., Calzetti, D., Moustakas, J., Murphy, E. J., Rieke, G. H., Bot, C., Hollenbach, D. J., Sheth, K., & Teplitz, H. I. 2007, *ApJ*, 663, 866  
 Draine, B. T. & Li, A. 2007, *ApJ*, 657, 810  
 Dwek, E. 1998, *ApJ*, 501, 643  
 Evans, II, N. J. 1999, *ARA&A*, 37, 311  
 Feldmann, R., Gnedin, N. Y., & Kravtsov, A. V. 2011, *ApJ*, 732, 115  
 Förster Schreiber, N. M. et al. 2009, *ApJ*, 706, 1364  
 Fumagalli, M., Krumholz, M. R., & Hunt, L. K. 2010, *ApJ*, 722, 919  
 Genzel, R., Tacconi, L. J., Gracia-Carpio, J., Sternberg, A., Cooper, M. C., Shapiro, K., Bolatto, A., Bouché, N., Bournaud, F., Burkert, A., Combes, F., Comerford, J., Cox, P., Davis, M., Schreiber, N. M. F., Garcia-Burillo, S., Lutz, D., Naab, T., Neri, R., Omont, A., Shapley, A., & Weiner, B. 2010, *MNRAS*, 407, 2091

- Genzel, R. et al. 2006, *Nature*, 442, 786
- Glover, S. C. O., Federrath, C., Mac Low, M., & Klessen, R. S. 2010, *MNRAS*, 404, 2
- Glover, S. C. O. & Mac Low, M.-M. 2011, *MNRAS*, 412, 337
- Gnedin, N. Y. & Kravtsov, A. V. 2010, *ApJ*, 714, 287
- Gnedin, N. Y., Tassis, K., & Kravtsov, A. V. 2009, *ApJ*, 697, 55
- Goldsmith, P. F. 2001, *ApJ*, 557, 736
- Groves, B., Dopita, M. A., Sutherland, R. S., Kewley, L. J., Fischer, J., Leitherer, C., Brandl, B., & van Breugel, W. 2008, *ApJS*, 176, 438
- Groves, B. A., Dopita, M. A., & Sutherland, R. S. 2004, *ApJS*, 153, 9
- Hayward, C. C., Kereš, D., Jonsson, P., Narayanan, D., Cox, T. J., & Hernquist, L. 2011, *arXiv/1101.0002*
- Hayward, C. C., Narayanan, D., Jonsson, P., Cox, T. J., Kereš, D., Hopkins, P. F., & Hernquist, L. 2010, *Conference Proceedings for UP2010: Have Observations Revealed a Variable Upper End of the Initial Mass Function?* Treyer, Lee, Seibert, Wyder, Neil eds. *arXiv/1008.4584*
- Hernquist, L. 1990, *ApJ*, 356, 359
- Heyer, M., Krawczyk, C., Duval, J., & Jackson, J. M. 2009, *ApJ*, 699, 1092
- Hinz, J. L. & Rieke, G. H. 2006, *ApJ*, 646, 872
- Hollenbach, D. J. & Tielens, A. G. G. M. 1999, *Reviews of Modern Physics*, 71, 173
- Hopkins, P. F., Cox, T. J., & Hernquist, L. 2008a, *ApJ*, 689, 17
- Hopkins, P. F. & Hernquist, L. 2010, *MNRAS*, 402, 985
- Hopkins, P. F., Lidz, A., Hernquist, L., Coil, A. L., Myers, A. D., Cox, T. J., & Spergel, D. N. 2007a, *ApJ*, 662, 110
- Hopkins, P. F., Richards, G. T., & Hernquist, L. 2007b, *ApJ*, 654, 731
- Hopkins, P. F., Younger, J. D., Hayward, C. C., Narayanan, D., & Hernquist, L. 2010, *MNRAS*, 402, 1693
- Hopkins, P. F. et al. 2005a, *ApJ*, 625, L71
- . 2005b, *ApJ*, 630, 705
- . 2006, *ApJS*, 163, 1
- . 2008b, *ApJS*, 175, 356
- . 2008c, *ApJS*, 175, 390
- . 2008d, *ApJ*, 679, 156
- . 2009, *ApJS*, 181, 135
- Israel, F. P. 2005, *A&A*, 438, 855
- Jonsson, P. 2006, *MNRAS*, 372, 2
- Jonsson, P., Groves, B. A., & Cox, T. J. 2010, *MNRAS*, 186
- Jonsson, P. & Primack, J. R. 2010, *New Astronomy*, 15, 509
- Joung, M. R., Mac Low, M., & Bryan, G. L. 2009, *ApJ*, 704, 137
- Juneau, S., Narayanan, D. T., Moustakas, J., Shirley, Y. L., Bussmann, R. S., Kennicutt, R. C., & Vanden Bout, P. A. 2009, *ApJ*, 707, 1217
- Juvela, M. 2005, *A&A*, 440, 531
- Kennicutt, Jr., R. C. 1998a, *ARA&A*, 36, 189
- . 1998b, *ApJ*, 498, 541
- Kennicutt, Jr., R. C. et al. 2003, *PASP*, 115, 928
- Krumholz, M. R. & Gnedin, N. Y. 2011, *ApJ*, 729, 36
- Krumholz, M. R., Leroy, A. K., & McKee, C. F. 2011, *ApJ*, 731, 25
- Krumholz, M. R., Matzner, C. D., & McKee, C. F. 2006, *ApJ*, 653, 361
- Krumholz, M. R., McKee, C. F., & Tumlinson, J. 2008, *ApJ*, 689, 865
- . 2009a, *ApJ*, 693, 216
- . 2009b, *ApJ*, 699, 850
- Krumholz, M. R. & Thompson, T. A. 2007, *ApJ*, 669, 289
- Kutner, M. L. & Leung, C. M. 1985, *ApJ*, 291, 188
- Larson, R. B. 1981, *MNRAS*, 194, 809
- Le Floch, E., Papovich, C., Dole, H., Bell, E. F., Lagache, G., Rieke, G. H., Egami, E., Pérez-González, P. G., Alonso-Herrero, A., & Rieke, M. J. 2005, *ApJ*, 632, 169
- Lee, H., Bettens, R. P. A., & Herbst, E. 1996, *A&AS*, 119, 111
- Leech, J., Isaak, K. G., Papadopoulos, P. P., Gao, Y., & Davis, G. R. 2010, *MNRAS*, 406, 1364
- Lemaster, M. N. & Stone, J. M. 2008, *ApJ*, 682, L97
- Leroy, A., Bolatto, A., Walter, F., & Blitz, L. 2006, *ApJ*, 643, 825
- Leroy, A. K., Bolatto, A., Gordon, K., Sandstrom, K., Gratier, P., Rosolowsky, E., Engelbracht, C. W., Mizuno, N., Corbelli, E., Fukui, Y., & Kawamura, A. 2011, *arXiv/1102.4618*
- Liszt, H. S., Pety, J., & Lucas, R. 2010, *A&A*, 518, A45+
- Maloney, P. & Black, J. H. 1988, *ApJ*, 325, 389
- Mao, R., Schulz, A., Henkel, C., Mauersberger, R., Muters, D., & Dinh-V-Trung. 2010, *ApJ*, 724, 1336
- McKee, C. F. & Krumholz, M. R. 2010, *ApJ*, 709, 308
- McKee, C. F. & Ostriker, E. C. 2007, *ARA&A*, 45, 565
- McKee, C. F. & Ostriker, J. P. 1977, *ApJ*, 218, 148
- Meier, D. S., Turner, J. L., Beck, S. C., Gorjian, V., Tsai, C., & Van Dyk, S. D. 2010, *AJ*, 140, 1294
- Mihos, J. C. & Hernquist, L. 1994, *ApJ*, 431, L9
- . 1996, *ApJ*, 464, 641
- Mo, H. J., Mao, S., & White, S. D. M. 1998, *MNRAS*, 295, 319
- Mühle, S., Henkel, C., de Maio, T., & Seaquist, E. R. 2011, *arXiv/1101.1262*
- Narayanan, D., Cox, T. J., Hayward, C. C., Younger, J. D., & Hernquist, L. 2009, *MNRAS*, 400, 1919
- Narayanan, D., Cox, T. J., & Hernquist, L. 2008a, *ApJ*, 681, L77
- Narayanan, D., Cox, T. J., Kelly, B., Davé, R., Hernquist, L., Di Matteo, T., Hopkins, P. F., Kulesa, C., Robertson, B., & Walker, C. K. 2008b, *ApJS*, 176, 331
- Narayanan, D., Cox, T. J., Robertson, B., Davé, R., Di Matteo, T., Hernquist, L., Hopkins, P., Kulesa, C., & Walker, C. K. 2006a, *ApJ*, 642, L107
- Narayanan, D., Cox, T. J., Shirley, Y., Davé, R., Hernquist, L., & Walker, C. K. 2008c, *ApJ*, 684, 996
- Narayanan, D., Dey, A., Hayward, C. C., Cox, T. J., Bussmann, R. S., Brodwin, M., Jonsson, P., Hopkins, P. F., Groves, B., Younger, J. D., & Hernquist, L. 2010a, *MNRAS*, 407, 1701
- Narayanan, D., Groppi, C. E., Kulesa, C. A., & Walker, C. K. 2005, *ApJ*, 630, 269
- Narayanan, D., Hayward, C. C., Cox, T. J., Hernquist, L., Jonsson, P., Younger, J. D., & Groves, B. 2010b, *MNRAS*, 401, 1613
- Narayanan, D., Kulesa, C. A., Boss, A., & Walker, C. K. 2006b, *ApJ*, 647, 1426
- Noeske, K. G. et al. 2007a, *ApJ*, 660, L47
- . 2007b, *ApJ*, 660, L43
- Obreschkow, D., Croton, D., De Lucia, G., Khochfar, S., & Rawlings, S. 2009, *ApJ*, 698, 1467
- Obreschkow, D. & Rawlings, S. 2009, *ApJ*, 696, L129
- Offner, S. S. R., Klein, R. I., McKee, C. F., & Krumholz, M. R. 2009, *ApJ*, 703, 131
- Oka, T., Hasegawa, T., Hayashi, M., Handa, T., & Sakamoto, S. 1998, *ApJ*, 493, 730
- Ostriker, E. C., McKee, C. F., & Leroy, A. K. 2010, *ApJ*, 721, 975
- Ostriker, E. C. & Shetty, R. 2011, *ApJ*, 731, 41
- Ostriker, E. C., Stone, J. M., & Gammie, C. F. 2001, *ApJ*, 546, 980
- Padoan, P. & Nordlund, Å. 2002, *ApJ*, 576, 870
- Papadopoulos, P. P. 2010, *ApJ*, 720, 226

Papadopoulos, P. P., Thi, W., Miniati, F., & Viti, S. 2010, arXiv/1009.2496

Pelupessy, F. I. & Papadopoulos, P. P. 2009, ApJ, 707, 954

Pelupessy, F. I., Papadopoulos, P. P., & van der Werf, P. 2006, ApJ, 645, 1024

Pety, J., Liszt, H. S., & Lucas, R. 2011, arXiv/1102.4667

Price, D. J., Federrath, C., & Brunt, C. M. 2011, ApJ, 727, L21+

Robertson, B., Yoshida, N., Springel, V., & Hernquist, L. 2004, ApJ, 606, 32

Robertson, B. et al. 2006, ApJ, 641, 21

Robertson, B. E. & Kravtsov, A. V. 2008, ApJ, 680, 1083

Rosolowsky, E., Engargiola, G., Plambeck, R., & Blitz, L. 2003, ApJ, 599, 258

Schöier, F. L., van der Tak, F. F. S., van Dishoeck, E. F., & Black, J. H. 2005, A&A, 432, 369

Scoville, N. Z., Yun, M. S., & Bryant, P. M. 1997, ApJ, 484, 702

Shetty, R., Glover, S. C., Dullemond, C. P., & Klessen, R. S. 2011a, MNRAS, 412, 1686

Shetty, R., Glover, S. C., Dullemond, C. P., Ostriker, E. C., Harris, A. I., & Klessen, R. S. 2011b, arXiv/1104.3695

Shetty, R. & Ostriker, E. C. 2008, ApJ, 684, 978

Snyder, G. F., Cox, T. J., Hayward, C. C., Hernquist, L., & Jonsson, P. 2011, arXiv/1102.3689

Solomon, P. M., Downes, D., Radford, S. J. E., & Barrett, J. W. 1997, ApJ, 478, 144

Solomon, P. M., Rivolo, A. R., Barrett, J., & Yahil, A. 1987, ApJ, 319, 730

Springel, V. 2000, MNRAS, 312, 859

—. 2005, MNRAS, 364, 1105

Springel, V., Di Matteo, T., & Hernquist, L. 2005a, ApJ, 620, L79

—. 2005b, MNRAS, 361, 776

Springel, V. & Hernquist, L. 2002, MNRAS, 333, 649

—. 2003, MNRAS, 339, 289

Sternberg, A. & Dalgarno, A. 1995, ApJS, 99, 565

Strong, A. W. & Mattox, J. R. 1996, A&A, 308, L21

Tacconi, L. J. et al. 2008, ApJ, 680, 246

Tan, J. C. 2000, ApJ, 536, 173

Teyssier, R., Chapon, D., & Bournaud, F. 2010, ApJ, 720, L149

van Zadelhoff, G., Dullemond, C. P., van der Tak, F. F. S., Yates, J. A., Doty, S. D., Ossenkopf, V., Hogerheijde, M. R., Juvela, M., Wiesemeyer, H., & Schöier, F. L. 2002, A&A, 395, 373

Vladilo, G. 1998, ApJ, 493, 583

Walker, C. K., Narayanan, G., & Boss, A. P. 1994, ApJ, 431, 767

Wall, W. F. 2007, MNRAS, 379, 674

Weingartner, J. C. & Draine, B. T. 2001, ApJ, 548, 296

Wilson, C. D. 1995, ApJ, 448, L97+

Wolfire, M. G., Hollenbach, D., & McKee, C. F. 2010, ApJ, 716, 1191

Xu, X., Narayanan, D., & Walker, C. 2010, ApJ, 721, L112

Yao, L., Seaquist, E. R., Kuno, N., & Dunne, L. 2003, ApJ, 588, 771

Younger, J. D., Hayward, C. C., Narayanan, D., Cox, T. J., Hernquist, L., & Jonsson, P. 2009, MNRAS, 396, L66

## APPENDIX A: EFFECTS OF PARAMETER CHOICES AND ASSUMPTIONS

In § 2, we outlined a number of parameter choices which could potentially influence the results in this paper. Here, we discuss the results in the context of these assumptions.

### A1 Self-Consistency of The Temperature Calculations

First, there is a discrepancy between the way the dust temperature is calculated in SUNRISE and in our temperature equilibrium model. In the former, the dust temperature is assumed to be in equilibrium with the radiation field, but we do not take into account any thermal exchange between the gas and dust. In the temperature equilibrium model, the dust grains are assumed to be able to exchange energy with the gas, but we hold the ambient radiation field fixed, rather than allowing it to change as the dust temperature does. Given the importance of the dust temperature in raising the gas temperature in this model, it is worth investigating any potential differences between the two dust temperatures.

In Figure A1, we plot the ratio of  $T_{\text{dust}}$  from SUNRISE compared to  $T_{\text{dust}}$  from the temperature equilibrium model as a function of GMC density<sup>9</sup> for our fiducial merger. There is generally good agreement between the two, though some number of points at higher densities deviate strongly from unity. The gas which has poor agreement between the two dust temperature calculations almost exclusively has all of its carbon in atomic form, rather than molecular. Beyond this, this gas tends to be towards the outskirts of the galaxy, in rather large cells in the adaptive mesh with relatively low masses ( $\sim 10 M_{\odot}$ ). Because we enforce a rule that clouds must have a minimum surface density of  $100 M_{\odot} \text{ pc}^{-2}$ , these regions have extremely high densities, even if relatively low mass. In atomic gas of this density, the gas couples with the dust and can cause the dust temperature to change from that of the background radiation field. These outlying points have little effect on the final results, however, as they contain rather little mass. We denote the 95th mass percentile by the blue shaded region in Figure A1. That is, the sum of the mass in the points outside of the blue region accounts for  $< 5\%$  of the total molecular mass in the galaxy. As is shown, the differences in the two dust temperatures are small in this shaded region.

### A2 SUNRISE Input Parameters

Similarly, a number of our assumptions in the SUNRISE modeling can have an effect on the derived dust temperature. We investigate those here. The important figure for these tests is Figure A2. Referring to § 2.3, the time-averaged covering fraction of birthclouds around stellar clusters is a free parameter. While we chose a modest covering fraction, it is possible that a larger fraction may be reasonable. For example, if we choose a fraction  $f_{\text{PDR}} = 1$ , the O and B stars would be blanketed by the ISM for their entire lives. This situation may exist in ULIRGs. To test for the effect in varying  $f_{\text{PDR}}$ , we plot the ratio of the dust temperatures derived from SUNRISE for a model with  $f_{\text{PDR}} = 1$  over the dust temperature from our fiducial model with  $f_{\text{PDR}} = 0.3$  against GMC density. The blue shaded region shows the 95th mass percentile, and grey

<sup>9</sup> This is not the actual mean density of the GMC, but the density accounting for an enhancement by the turbulent compression of gas. This is the density that is used in the temperature equilibrium calculation.



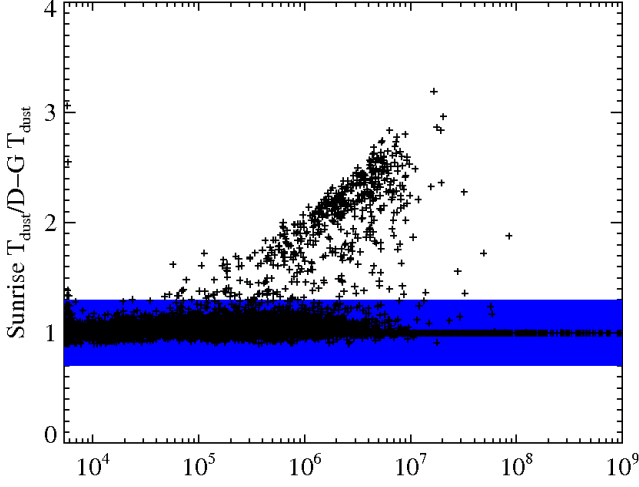


**Figure A1.** Comparison between the SUNRISE dust temperatures and those calculated from the temperature equilibrium calculation as a function of density for model GMCs in our fiducial merger. See text for details.

denotes the 99th mass percentile. The model with a larger clearing timescale for the birthclouds has cooler dust temperatures as less UV flux interacts with the ISM. However, the differences in dust temperature are generally within a factor of 50%, and much less than that ( $< 10\%$ ) when considering the bulk of the mass of the galaxy. We conclude that the PDR covering fraction is not an important driver in our model results.

We can explore the effect of discarding the PDR birthcloud model, and assuming the cold ISM has a uniform volume filling fraction. In this case, the UV photons escape the star particles easily, though optical depths for the photons in the ISM are large. For some number of the clouds outside of the nuclear region, the dust temperatures are thus colder than in our fiducial model (the low ratio points in Figure A2). However, the bulk of the gas mass is in a confined nuclear region in the galaxy which sees the intense UV radiation field. Because of this, this dust is heated well, and has comparable dust temperatures to our fiducial model. The dispersion in dust temperatures is again within 50%, and the 95th% percentile of mass shows relatively small discrepancies.

It is possible that the AGN in the model merger contributes strongly to the dust temperature. To test this, we investigate a model where we have turned off the contribution of the AGN in determining the dust temperature in the merger. While it is difficult to see by eye, the dust temperatures in the model with the AGN are hotter than the model with no AGN. By and large, however, the AGN is not powerful enough to have a significant effect on the overall temperature structure of the cold ISM as noted by the blue and grey shaded regions.

### A3 GADGET-3 Input Parameters

We now turn to possible parameters in the hydrodynamics simulations which may affect our results. As described in § 2.1, we make a number of parameter choices which may affect the star formation history of the model galaxies. Because the gas densities and dust and gas temperature can depend on these assumptions, it is worth exploring the robustness of our model results in the context of these choices.

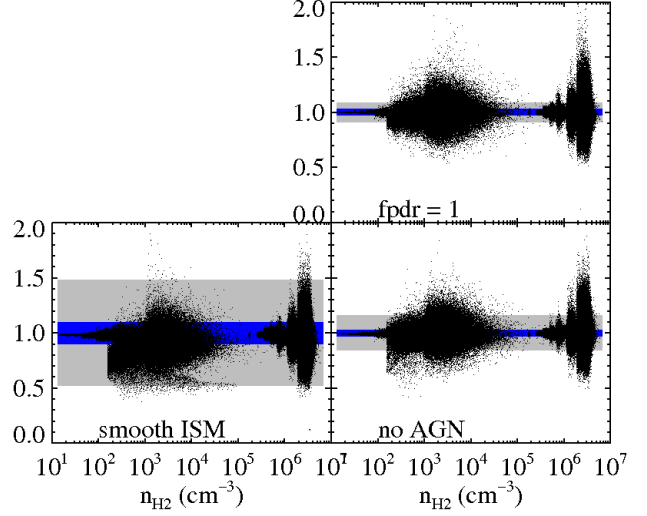


**Figure A2.** Ratio of  $T_{\text{dust}}$  under various subresolution ISM specifications to that derived in our fiducial model versus  $\text{H}_2$  density in model GMCs. See text for details.

There are two principle parameter choices which govern the physical state of the ISM in our hydrodynamic modes: the star formation “law”, and the equation of state. As discussed in § 2.1, we adopt a star formation law such that the star formation time scale is assumed to be proportional to the local dynamical timescale, and whose rate matches the normalisation of the locally observed Kennicutt (1998a) relation.

In the absence of a complete theory of star formation, a number of possible choices exist regarding the implementation of a star formation recipe on subresolution scales. One can imagine a similar Kennicutt-Schmidt solution, though with an index of unity as appears to be observed on resolved scales in nearby galaxies (Bigiel et al. 2008), or steeper index as tentative observational (Bouché et al. 2007) and theoretical (Feldmann et al. 2011) evidence motivates at high-redshift. Beyond this, more sophisticated physical models may provide reasonable prescriptions for star formation in galaxy evolution models (e.g. Tan 2000; Krumholz et al. 2009b; Ostriker et al. 2010). While it is outside the scope of this study to perform a detailed study of various star formation recipes in GADGET-3, we perform some simple tests to investigate the role of our adopted star formation law in driving the simulated  $X_{\text{CO}}$  factors.

In the Table, we show the luminosity-weighted mean  $X_{\text{CO}}$  values for our fiducial merger during the peak of their starburst for a variety of input parameters in our GADGET-3 simulations. The Kennicutt-Schmidt index=2 case shows a comparable  $X_{\text{CO}}$  value as the fiducial merger. While the burst is moderately diminished (owing to rapid consumption of the gas during early phases of the merger’s evolution, though still quite large at  $\sim 250 \text{ M}_{\odot} \text{ yr}^{-1}$  as opposed to  $\sim 340 \text{ M}_{\odot} \text{ yr}^{-1}$  in the fiducial merger), the large stellar mass upon coalescence maintains a large velocity dispersion in the gas. This drives a low mean  $X_{\text{CO}}$ .

The model with the largest impact on our results is the model with Kennicutt-Schmidt index=1; This model merger has a mean  $X_{\text{CO}}$  comparable to the model disc. Models with a KS index of 1 do not go through a burst upon merging (T. Cox, private communi-



cation). With a KS index of 1, to first order, the total star formation rate is proportional to the total gas mass. Because we don't include any gas replenishment from the intergalactic medium, the gas mass only decreases with time, as does the SFR in this simulation. The low SFR upon merging leads to low gas/dust temperatures, and increased  $X_{\text{CO}}$ . We note that this situation is unlikely to describe real mergers as, observationally, galaxy mergers exhibit the highest star formation rates in the local Universe. Both observational (Bigiel et al. 2008) and theoretical (Krumholz et al. 2009b; Ostriker & Shetty 2011) evidence suggest that a KS index  $> 1$  may describe high-surface density systems.

We utilise an equation of state for the ISM which incorporates a subresolution prescription for capturing the effect of supernovae heating of the ISM (Springel & Hernquist 2003). The nominal Springel & Hernquist (2003) and Springel et al. (2005b) EOS is given by:

$$P_{\text{eff}} = (\gamma - 1)(\rho_h u_h + \rho_c u_c) \quad (\text{A1})$$

where  $\gamma = 5/3$  as the adiabatic index of the gas,  $\rho_{h,c}$  is the density of the hot and cold phase, and  $u_{h,c}$  is the specific thermal energy of the two phases. For a given IMF, Springel & Hernquist (2003) show that the EOS is completely defined by the star formation time scale, the normalisation of the cloud evaporation rate, and a supernovae “temperature” which defines the heating rate from supernovae of a given IMF. The full “effective” EOS has the property in which pressure rises with density faster than an isothermal gas, as can be seen in Figure 4 of Springel et al. (2005b).

Our fiducial model utilises a softer EOS than the full model. In particular, we interpolate between the full “stiff” model (where we assign a parameter  $q_{\text{EOS}} = 1$ ) and isothermal model ( $q_{\text{EOS}} = 0$ ) and employ  $q_{\text{EOS}} = 0.25$ . In the full “stiff” EOS as in simulations of discs scaled for the local Universe, the ISM can become so pressurised as to appear smooth with relatively few clumps (Springel et al. 2005b). To test our assumption of a softer EOS, we have run a test simulation with  $q_{\text{EOS}}=1$ .

In the Table, we show the mean  $X_{\text{CO}}$  for our fiducial merger, though with  $q_{\text{EOS}}=1$  (denoted “Stiff EOS”). We see a larger value than the fiducial model. Isolating the root cause is nontrivial. By effectively increasing the effect of supernovae feedback, we increase dust heating (by reducing the clumpiness of the gas), though we also reduce the magnitude of the burst (due to a retardation of gas fragmentation). These effects serve to somewhat offset one another with respect to the gas temperature.

We test whether our assumption of  $G_0 = 1$  outside of clouds plays a strong role in our model results. Following Ostriker et al. (2010), we have run a model in which we scale the interstellar radiation field by the value of the local SFR compared to that in the solar neighbourhood, and show the mean  $X_{\text{CO}}$  value in the Table (denoted by “OML G-Scaling”). Because the clouds are strongly shielded in this model, scaling  $G$  makes little difference.

Finally, we consider the spatial resolution of our model. Our current resolution has cell sizes ( $\sim 70$  pc) which are of order the SPH smoothing length. Further increasing the spatial resolution does not provide new physical information. More seriously, increasing the spatial resolution of the SPH simulations would run into scenarios of unphysical descriptions of the ISM with the Springel & Hernquist (2003) multiphase model. We can see, however, what direction the results may go if it were possible to increase our resolution. To investigate this, we have run our fiducial merger snapshot with one less level of refinement in the adaptive mesh, giving a minimum cell size of  $\sim 140$  pc, and show the mean  $X_{\text{CO}}$  in the Table (denoted by “Half-Res”). The mean  $X_{\text{CO}}$  in the

**Table A1.**

Model	Mean $X_{\text{CO}}$ ( $\text{cm}^{-2}/\text{K-km s}^{-1}$ )
Fiducial	$6.31 \times 10^{19}$
Stiff EOS	$1.08 \times 10^{20}$
KS = 2	$5.43 \times 10^{19}$
KS = 1	$2.73 \times 10^{20}$
OML G-scaling	$7.10 \times 10^{19}$
Half-Res	$3.02 \times 10^{19}$

low resolution model is 60% the value of the fiducial model. It is conceivable, then, that further increasing the spatial resolution would increase  $X_{\text{CO}}$  in the merger model. On the other hand, reducing the cell size would result in more resolved GMCs. Because it is the resolved GMCs that drive the mean  $X_{\text{CO}}$  for the merger model, it is also possible that increased spatial resolution would result in little change to the results presented here.